


# Imprints of Einstein-Maxwell-dilaton-axion gravity in the observed shadows of Sgr A\* and M87\*

Siddharth Kumar Sahoo<sup>✉,\*</sup>, Neeraj Yadav,<sup>†</sup> and Indrani Banerjee<sup>‡</sup>

*Department of Physics and Astronomy, National Institute of Technology, Rourkela, Odisha-769008 India*

 (Received 29 May 2023; revised 18 August 2023; accepted 20 December 2023; published 5 February 2024)

Einstein-Maxwell-dilaton-axion (EMDA) gravity provides a simple framework to investigate the signatures of string theory. The axion and the dilaton fields arising in EMDA gravity have important implications in inflationary cosmology and in addressing the late time acceleration of the Universe. It is therefore instructive to explore the implications of such a model in explaining the astrophysical observations. The Kerr-Sen metric represents the exact, stationary, and axisymmetric black hole solution of EMDA gravity. Such a black hole is characterized by the angular momentum  $a$  acquired from the axionic field and the dilatonic charge  $r_2$  arising from string compactifications. We study the role of spin and the dilaton parameter in modifying the shape and size of the black hole critical curve, which is associated with the projection of the spherical null geodesics on the sky. We compare the theoretically derived critical curve with the Event Horizon Telescope results related to the images of M87\* and Sgr A\* to obtain constraints on the dilaton parameter  $r_2$ . We take into account the errors in mass and distance of M87\* and Sgr A\* while deriving their theoretical critical curve. Our analysis reveals that the image of M87\* exhibits a preference toward the Kerr scenario when the critical curve angular diameter is calculated with the central value of mass and distance. When errors in mass and distance are taken into account the allowed range of  $r_2$  turns out to be  $0 \lesssim r_2 \lesssim 1$ . For Sgr A\*, the preferred range of  $r_2$  is  $0.1 \lesssim r_2 \lesssim 0.4$  when central values of mass and distance are used to calculate the theoretical critical curve. When error bars in mass and distance are used to calculate the theoretical critical curve of Sgr A\*, the preferred range of  $r_2$  turns out to be  $0 \lesssim r_2 \lesssim 0.5$ . Thus the image of M87\* favors the Kerr scenario and allows the Kerr-Sen scenario only when errors in the mass and distance are taken into consideration while the image of Sgr A\* favors the Kerr-Sen scenario and allows general relativity when errors in the mass and distance are taken into account.

DOI: [10.1103/PhysRevD.109.044008](https://doi.org/10.1103/PhysRevD.109.044008)

## I. INTRODUCTION

General relativity (GR), the successor of Newtonian theory of gravity has radically changed our understanding pertaining to gravitational interaction. In GR, the mass of a body produces curvature in the spacetime which changes the metric of the spacetime from the Minkowski metric [1]. The particles in curved spacetime move along geodesics which are obtained by solving the geodesic equation associated with the metric describing the spacetime. The metric itself is obtained by solving the Einstein field equations and depends crucially on the matter distribution. GR has many interesting predictions [1], namely, the perihelion precession of mercury, the bending of light, and the gravitational redshift of radiation from distant stars, to name a few, which have been experimentally verified [2,3]. The detection of gravitational waves by the LIGO-VIRGO Collaboration [4–6] and the release of black hole

images of M87\* and Sgr A\* by the Event Horizon Telescope Collaboration [7–18] have further demonstrated GR as a successful theory of gravity.

Despite being a very successful theory, GR also has certain limitations. The theory allows the formation of singularities [19–21] namely, the black hole and the big bang singularities where the theory loses its predictive power [19,20,22,23]. This indicates that GR is not a complete theory of gravity [2] and that at very small length scales it must receive considerable corrections from a more complete theory that incorporates its quantum nature [24–28]. In the observational front, GR falls short in explaining the nature of dark matter [29–31] and dark energy [32–38], which are invoked to explain the flat rotation curves of galaxies and the accelerated expansion of the Universe, respectively. These inadequacies have led to the development of many alternate theories of gravity which address the limitations of GR [39–47] and deviate from GR in the strong field regime. Therefore, to test the effectiveness of alternative theories of gravity, it is necessary to study how effectively they explain observations related to strong field tests of gravity [48,49].

\*521ph1007@nitrrkl.ac.in

†418ph5062@nitrrkl.ac.in

‡banerjeein@nitrrkl.ac.in

The alternatives to GR include higher curvature gravity, e.g.,  $f(R)$  gravity, [50–52] and Lanczos Lovelock models [53–56], extra dimensional models [57–63], and scalar-tensor/scalar-vector-tensor theories of gravity [64–68]. Many of these models are string inspired which provide a framework for force unification [69–72]. In this work we intend to discern the signatures of the string inspired model, namely, the Einstein-Maxwell-dilaton-axion (EMDA) gravity, from observations related to black hole images. EMDA, a scalar-vector-tensor theory of gravity, arises in the low energy effective action of superstring theories [73] on compactifying the ten-dimensional heterotic string theory on a six-dimensional torus. In the EMDA theory, the scalar field dilaton and the pseudoscalar axion are coupled to the Maxwell field and the metric. The axion and dilaton fields which originate from string compactifications have interesting implications in inflationary cosmology and the late-time acceleration of the Universe [74,75]. It is therefore important to explore the footprints of EMDA gravity in astrophysical observations which is the goal of the present work.

In particular, we aim to decipher the possible imprints of the dilaton charge associated with black holes, from estimates related to black hole images. Black holes (BH) are compact objects with extremely strong gravity. Among the various systems that possess strong gravitational field, black holes are the most interesting and the simplest ones. Different black hole solutions have been constructed in the context of string inspired low-energy effective theories [76–79]. Interestingly, the charge neutral axisymmetric black hole solution in string theory resembles the Kerr solution in GR [80,81]. In EMDA gravity, the stationary and axisymmetric black hole solution is represented by the Kerr-Sen metric which is similar to the Kerr-Newman spacetime in GR. Despite the similarities, the intrinsic geometry of the two black holes varies considerably which has been explored extensively in the past [82–85].

Astrophysical signatures of the Kerr-Sen black hole have been studied previously in the context of photon motion, null geodesics, strong gravitational lensing, etc. [82,86–90]. The Kerr-Sen scenario has been tested using the reflection spectrum of black holes to estimate bounds on the dilaton charge [91]. In [90], the authors have worked out the critical curve of the Kerr-Sen black hole, but they have not compared their results with the observed images, and hence no constrain on the dilaton charge was reported. Recently, the critical curve of dyonic Kerr-Sen black holes has been studied [92], and an upper bound on the magnetic monopole charge of Sgr A\* has been mentioned. It is important to mention here that in most of the literature, the projection of null geodesics on the observer's sky is referred as the *shadow*, which we mention in our work as the *critical curve* (following [93]). The reason for not adopting this well-used terminology (black hole shadow) will be addressed in Sec. III. We explore the role of the dilaton charge in

modifying the structure of the black hole critical curve from that of the Kerr scenario. We compare the theoretically derived critical curve (which depends on the dilaton parameter, spin, and the angle of inclination) with that of the Event Horizon Telescope results of M87\* and Sgr A\*. Such a study enables us to establish constraints on the dilaton parameter of the Kerr-Sen black hole and allows us to comment on the possible feasibility of string theory in explaining the observed black hole images.

The structure of the paper is as follows: In Sec. II we give a brief overview of the Kerr-Sen BH. In Sec. III we derive the critical curve of the Kerr-Sen BH. In Sec. IV we discuss our results related to constraints on the dilaton parameter  $r_2$  from the EHT observed images of M87\* and Sgr A\*. We give a summary of our results and concluding remarks in Sec. V. In our paper we have chosen the metric signature  $(-, +, +, +)$  and used geometrized units ( $G = c = 1$ ).

## II. BLACK HOLE IN EINSTEIN-MAXWELL DILATON AXION GRAVITY

The EMDA gravity [73,94] results from the compactification of ten-dimensional heterotic string theory on a six-dimensional torus  $T^6$ . In EMDA gravity,  $N = 4$ ,  $d = 4$  supergravity is coupled to  $N = 4$  super Yang-Mills theory which can be suitably truncated to a pure supergravity theory exhibiting  $S$  and  $T$  dualities. The bosonic sector of this supergravity theory when coupled to the  $U(1)$  gauge field is known as the EMDA gravity [94] which provides a simple framework to study classical solutions. The four-dimensional effective action for EMDA gravity consists of a generalization of the Einstein-Maxwell action such that the metric  $g_{\mu\nu}$  is coupled to the dilaton field  $\chi$ , the  $U(1)$  gauge field  $A_\mu$ , and the Kalb-Ramond field strength tensor  $H_{\alpha\beta\gamma}$ . The action corresponding to EMDA gravity assumes the form

$$S = \frac{1}{16\pi} \int \sqrt{-g} d^4x \times \left( R - 2\partial_\mu \chi \partial^\mu \chi - \frac{1}{3} H_{\rho\sigma\delta} H^{\rho\sigma\delta} + e^{-2\chi} F_{\alpha\beta} F^{\alpha\beta} \right). \quad (1)$$

In Eq. (1)  $g$  is the determinant, and  $R$  the Ricci scalar associated with the four-dimensional metric  $g_{\mu\nu}$ .  $\chi$  represents the dilatonic field;  $F_{\mu\nu} = \nabla_\mu A_\nu - \nabla_\nu A_\mu$  is the Maxwell field strength tensor, and  $H_{\rho\sigma\delta}$  is given by

$$H_{\rho\sigma\delta} = \nabla_\rho B_{\sigma\delta} + \nabla_\sigma B_{\delta\rho} + \nabla_\delta B_{\rho\sigma} - A_\rho B_{\sigma\delta} - A_\sigma B_{\delta\rho} - A_\delta B_{\rho\sigma}, \quad (2)$$

where  $A_\mu$  is the vector potential and  $B_{\mu\nu}$  is the second rank antisymmetric tensor field called the Kalb-Ramond field while its cyclic permutation with  $A_\mu$  denotes the Chern-Simons term. In four dimensions the Kalb-Ramond field

strength tensor  $H_{\rho\sigma\delta}$  can be written in terms of the pseudoscalar axion field  $\psi$ , such that

$$H_{\alpha\beta\delta} = \frac{1}{2} e^{4\chi} \epsilon_{\alpha\beta\delta\gamma} \partial^\gamma \psi. \quad (3)$$

The action in Eq. (1) written in terms of the axion field assumes the form

$$S = \frac{1}{16\pi} \int \sqrt{-g} d^4x \left[ R - 2\partial_\nu \chi \partial^\nu \chi - \frac{1}{2} e^{4\chi} \partial_\nu \psi \partial^\nu \psi + e^{-2\chi} F_{\rho\sigma} F^{\rho\sigma} + \psi F_{\rho\sigma} \tilde{F}^{\rho\sigma} \right]. \quad (4)$$

Variation of the action with respect to the dilaton, axion, and Maxwell fields gives their corresponding equations of motion. By solving the aforesaid equations one obtains solutions for the dilaton, axion, and the Maxwell field, respectively [73,94,95],

$$e^{2\chi} = \frac{r^2 + a^2 \cos^2 \theta}{r(r + r_2) + a^2 \cos^2 \theta} \quad (5)$$

$$\psi = \frac{q^2}{M} \frac{a \cos \theta}{r^2 + a^2 \cos^2 \theta} \quad (6)$$

$$A = \frac{qr}{\Sigma} (-dt + a \sin^2 \theta d\phi), \quad (7)$$

where  $M$  is the mass,  $a$  is the spin, and  $q$  is the charge of the black hole. In Eq. (5)  $r_2$  is associated with the dilaton parameter and is given by  $r_2 = \frac{q^2}{M} e^{2\chi_0}$  where  $\chi_0$  represents the asymptotic value of the dilatonic field. The dilaton parameter also depends on the electric charge of the black hole, which owes its origin to the axion-photon coupling and not to the in-falling charged particles. This is because the axion and dilaton field strengths vanish if the electric charge  $q = 0$  [see Eqs. (6) and (5)]. It is further important to note that the axion field renders a nonzero spin to the black hole since the field strength corresponding to the axion field vanishes if the black hole is nonrotating [Eq. (6)].

Varying the action with respect to the metric gives the Einstein field equations,

$$G_{\mu\nu} = T_{\mu\nu}(F, \chi, \psi), \quad (8)$$

where  $G_{\mu\nu}$  is the Einstein tensor and  $T_{\mu\nu}$  the energy-momentum tensor which is given by

$$T_{\mu\nu}(F, \chi, \psi) = e^{2\chi} (4F_{\mu\rho} F_\nu^\rho - g_{\mu\nu} F^2) - g_{\mu\nu} \left( 2\partial_\gamma \chi \partial^\gamma \chi + \frac{1}{2} e^{4\chi} \partial_\gamma \psi \partial^\gamma \psi \right) + \partial_\mu \chi \partial_\nu \chi + e^{4\chi} \partial_\mu \psi \partial_\nu \psi. \quad (9)$$

The Kerr-Sen metric [73] is obtained when one looks for the stationary and axisymmetric solution of the aforesaid Einstein's equations [96–98]. In Boyer-Lindquist coordinates the Kerr-Sen metric takes the form

$$ds^2 = - \left( 1 - \frac{2Mr}{\tilde{\rho}} \right) dt^2 + \frac{\tilde{\rho}}{\Delta} (dr^2 + \Delta d\theta^2) - \frac{4aMr}{\tilde{\rho}} \sin^2 \theta dt d\phi + \sin^2 \theta d\phi^2 \left[ r(r + r_2) + a^2 + \frac{2Mra^2 \sin^2 \theta}{\tilde{\rho}} \right], \quad (10)$$

where

$$\tilde{\rho} = r(r + r_2) + a^2 \cos^2 \theta \quad (11a)$$

$$\Delta = r(r + r_2) - 2Mr + a^2. \quad (11b)$$

The nonrotating counterpart of the Kerr-Sen metric corresponds to a pure dilaton black hole characterized by its mass, electric charge, and asymptotic value of the dilaton field [77,99].

In order to obtain the event horizon  $r_h$  of the Kerr-Sen black hole one solves for  $g^{rr} = \Delta = 0$ , which gives

$$r_h = M - \frac{r_2}{2} + \sqrt{\left( M - \frac{r_2}{2} \right)^2 - a^2}. \quad (12)$$

Since  $r_2 = \frac{q^2}{M} e^{2\chi_0} > 0$ , the presence of a real, positive event horizon requires  $0 \leq \frac{r_2}{M} \leq 2$  [see Eq. (12)]. Since we are interested in black hole solutions we will be interested in this regime of  $r_2$  in this work.

### III. NULL GEODESICS IN THE KERR-SEN SPACETIME

In this section we investigate the motion of photons in the Kerr-Sen background. In particular, we will be interested in calculating the projection of the spherical null geodesics on the observer's sky. Following Gralla *et al.* [93] we shall refer to the curve associated with such a projection as the critical curve and not the black hole shadow. In what follows, we will compute the outline of the critical curve in EMDA gravity which in turn can be compared with the Kerr scenario in general relativity.

For a stationary, axisymmetric metric, the Lagrangian  $\mathcal{L}$  for the motion of any test particle is given by

$$\begin{aligned} \mathcal{L}(x^\mu, \dot{x}^\mu) &= \frac{1}{2} g_{\mu\nu} \dot{x}^\mu \dot{x}^\nu \\ &= \frac{1}{2} (g_{tt} \dot{t}^2 + g_{rr} \dot{r}^2 + g_{\theta\theta} \dot{\theta}^2 + g_{\phi\phi} \dot{\phi}^2 + 2g_{t\phi} \dot{t} \dot{\phi}). \end{aligned} \quad (13)$$

The action  $\mathcal{S}$  representing the motion of test particles satisfying the Hamilton-Jacobi equation is given by

$$\mathcal{H}(x^\nu, p_\nu) + \frac{\partial \mathcal{S}}{\partial \lambda} = 0, \quad (14)$$

where  $\mathcal{H}$  is the Hamiltonian,  $\lambda$  is a curve parameter, and  $p_\mu$ , the conjugate momentum corresponding to the coordinate  $x^\mu$  is

$$p_\mu = \frac{\partial \mathcal{S}}{\partial x^\mu} = \frac{\partial \mathcal{L}}{\partial \dot{x}^\mu} = g_{\mu\nu} \dot{x}^\nu. \quad (15)$$

The Hamiltonian is given by

$$\mathcal{H}(x^\nu, p_\nu) = \frac{1}{2} g^{\mu\nu} p_\mu p_\nu = \frac{k}{2} = 0, \quad (16)$$

where  $k$  denotes the rest mass of the test particle which is zero for photons. Since the Kerr-Sen metric does not explicitly depend on  $t$  and  $\phi$ , the first term in the Euler-Lagrange equation,

$$\frac{\partial \mathcal{L}}{\partial x^\mu} - \frac{d}{d\lambda} \left( \frac{\partial \mathcal{L}}{\partial \dot{x}^\mu} \right) = 0, \quad (17)$$

is zero. Therefore, the energy  $E$  and the angular momentum  $L_z$  of the photon are conserved. Using Eq. (15) these constants are given by

$$E = -g_{tt}\dot{t} - g_{t\phi}\dot{\phi} = -p_t, \quad L_z = g_{t\phi}\dot{t} + g_{\phi\phi}\dot{\phi} = p_\phi. \quad (18)$$

We further note from Eq. (15) that

$$p_t = \frac{\partial \mathcal{S}}{\partial t} = g_{tt}\dot{t} + g_{t\phi}\dot{\phi} = -E, \quad (19)$$

$$p_\phi = \frac{\partial \mathcal{S}}{\partial \phi} = g_{t\phi}\dot{t} + g_{\phi\phi}\dot{\phi} = L_z$$

$$p_r = \frac{\partial \mathcal{S}}{\partial r} = g_{rr}\dot{r}, \quad p_\theta = \frac{\partial \mathcal{S}}{\partial \theta} = g_{\theta\theta}\dot{\theta}. \quad (20)$$

Integrating Eq. (19) the action  $\mathcal{S}$  can be written as

$$\mathcal{S} = -Et + L_z\phi + \bar{\mathcal{S}}(r, \theta). \quad (21)$$

It turns out that  $\bar{\mathcal{S}}(r, \theta)$  can be separated into  $r$  and  $\theta$  giving us

$$\mathcal{S} = -Et + L_z\phi + \mathcal{S}^r(r) + \mathcal{S}^\theta(\theta). \quad (22)$$

From Eq. (16) we have  $g^{\mu\nu} p_\mu p_\nu = 0$  giving us

$$g^{tt} p_t^2 + g^{rr} p_r^2 + g^{\theta\theta} p_\theta^2 + g^{\phi\phi} p_\phi^2 + 2g^{t\phi} p_t p_\phi = 0. \quad (23)$$

Using Eq. (19), Eq. (20), and Eq. (22), Eq. (23) can be written as

$$g^{tt} E^2 - 2g^{t\phi} E L_z + g^{\phi\phi} L_z^2 + g^{rr} \left( \frac{d\mathcal{S}^r}{dr} \right)^2 + g^{\theta\theta} \left( \frac{d\mathcal{S}^\theta}{d\theta} \right)^2 = 0, \quad (24)$$

which on substitution of the metric components  $g^{\mu\nu}$  [see Eq. (10)] gives

$$\left[ \Delta a^2 \sin^2 \theta - (r(r+r_2) + a^2)^2 \right] \frac{E^2}{\Delta} + \frac{4MraEL_z}{\Delta} + \frac{L_z^2}{\Delta \sin^2 \theta} (\tilde{\rho} - 2Mr) + \Delta \left( \frac{d\mathcal{S}^r}{dr} \right)^2 + \left( \frac{d\mathcal{S}^\theta}{d\theta} \right)^2 = 0. \quad (25)$$

The above equation can be separated into  $r$  and  $\theta$  such that

$$\begin{aligned} & \Delta \left( \frac{d\mathcal{S}^r}{dr} \right)^2 + a^2 E^2 + L_z^2 - \frac{aL_z^2}{\Delta} \\ & - \frac{E^2}{\Delta} (r(r+r_2) + a^2)^2 + \frac{4MraL_z E}{\Delta} \\ & = - \left( \frac{d\mathcal{S}^\theta}{d\theta} \right)^2 + aE^2 \cos^2 \theta - L_z^2 \cot^2 \theta = -Q, \end{aligned} \quad (26)$$

where  $Q$  is called the Carter's constant. From Eq. (26) the angular part is given by

$$\left( \frac{d\mathcal{S}^\theta}{d\theta} \right) = \sqrt{Q - L_z^2 \cot^2 \theta + a^2 E^2 \cos^2 \theta} = \sqrt{\Theta(\theta)}, \quad (27)$$

where

$$Q - L_z^2 \cot^2 \theta + a^2 E^2 \cos^2 \theta = \Theta(\theta). \quad (28)$$

The radial equation is given by

$$\mathcal{V}(r) = \Delta^2 \left( \frac{d\mathcal{S}^r}{dr} \right)^2, \quad (29)$$

where

$$\begin{aligned} \mathcal{V}(r) = & -Q\Delta - a^2 E^2 \Delta + E^2 (r(r+r_2) + a^2)^2 \\ & + a^2 L_z^2 - \Delta L_z^2 - 4MraEL_z. \end{aligned} \quad (30)$$

We also note that

$$\dot{r} = p^r = g^{rr} \frac{d\mathcal{S}^r}{dr} = \frac{\Delta \sqrt{\mathcal{V}(r)}}{\tilde{\rho}} \quad (31)$$

while

$$\dot{\theta} = p^\theta = g^{\theta\theta} \frac{d\mathcal{S}^\theta}{d\theta} = \frac{\sqrt{\Theta(\theta)}}{\tilde{\rho}}. \quad (32)$$

Therefore the first order geodesic equations for  $r$  and  $\theta$  can be respectively written as

$$\begin{aligned} \left( \frac{\tilde{\rho}}{E} \right)^2 \dot{r}^2 = & a^2 \xi^2 + (r(r+r_2) + a^2)^2 \\ & - 4Mra\xi - \Delta(\eta + a^2 + \xi^2) \quad \text{and} \end{aligned} \quad (33)$$

$$\left(\frac{\tilde{\rho}}{E}\right)^2 \dot{\theta}^2 = \eta + a^2 \cos^2 \theta - \xi^2 \cot^2 \theta, \quad (34)$$

where  $\xi = L_z/E$  and  $\eta = Q/E^2$  represent the two impact parameters. While  $\xi$  denotes the distance from the axis of rotation,  $\eta$  signifies the distance from the equatorial plane.

The first order geodesic equations for  $t$  and  $\phi$  are obtained from Eq. (19) and are given by

$$\dot{t} = \frac{E[(r+r_2)r+a^2]^2 - \Delta a^2 \sin^2 \theta}{\tilde{\rho} \Delta} - \frac{2MarL_z}{\tilde{\rho} \Delta} \quad (35)$$

$$\dot{\phi} = \left(\frac{\tilde{\rho} - 2Mr}{\tilde{\rho} \Delta}\right) \frac{L_z}{\sin^2 \theta} + \frac{2MraE}{\tilde{\rho} \Delta}. \quad (36)$$

### A. Analysis of the $\theta$ equation

In this section we simplify the angular equation of motion by defining a new variable  $u = \cos \theta$ . Then the angular Eq. (34) is given by

$$\left(\frac{\tilde{\rho}}{E}\right)^2 \dot{u}^2 = \eta - u^2(\eta + \xi^2 - a^2) - a^2 u^4 = \mathcal{G}(u(\theta)). \quad (37)$$

Note that the left-hand side of Eq. (37) is positive which implies that the right-hand side also needs to be positive. Since  $\mathcal{G}(1) = -\xi^2$  is negative, the photon cannot access  $\theta = 0$ . To obtain the maximum accessible value of  $\theta$  denoted by  $\theta_{\max}$  we solve for  $\mathcal{G}(u) = 0$  which gives

$$u^2 = \frac{-(\eta + \xi^2 - a^2) \pm \sqrt{(\eta + \xi^2 - a^2)^2 + 4a^2\eta}}{2a^2}. \quad (38)$$

If  $\eta > 0$  one can only consider the positive root of (38) since the left-hand side of Eq. (38) is positive. Such orbits cross the equatorial plane reaching a maximum height of  $\theta_{\max}$  given by the solution of Eq. (38). For negative  $\eta$ , we define  $\eta = -|\eta|$  such that Eq. (38) can be rewritten as

$$u^2 = \frac{|\eta| - \xi^2 + a^2 \pm \sqrt{(-|\eta| + \xi^2 - a^2)^2 - 4a^2|\eta|}}{2a^2}. \quad (39)$$

From Eq. (39) it is easy to note that for its right-hand side to be positive,

$$a^2 + |\eta| - \xi^2 > 0, \quad (40)$$

which is the condition to be satisfied by the impact parameters.

Finally, we note that  $\eta = 0$  has two solutions, namely,

$$u_1^2 = 0 \quad u_2^2 = 1 - \left(\frac{\xi^2}{a^2}\right). \quad (41)$$

If  $\xi^2 > a^2$  only  $u_1^2$  is valid else both  $u_1^2$  and  $u_2^2$  are valid solutions.

### B. Analysis of the radial equation

In this section we consider the geodesic equation associated with the radial coordinate given by Eq. (33),

$$\begin{aligned} \left(\frac{\tilde{\rho}}{E}\right)^2 \dot{r}^2 &= a^2 \xi^2 + (r(r+r_2) + a^2)^2 - 4Mra\xi \\ &- \Delta(\eta + a^2 + \xi^2) = \tilde{V}(r). \end{aligned} \quad (42)$$

We will be interested in spherical photon orbits of constant radius which yields  $\tilde{V}(r) = \tilde{V}'(r) = 0$ . Thus, we have to solve the following two equations for  $\eta$  and  $\xi$ :

$$a^2 \xi^2 + (r(r+r_2) + a^2)^2 - 4Mra\xi - \Delta(\eta + a^2 + \xi^2) = 0 \quad (\text{obtained from } \tilde{V}(r) = 0)$$

$$2(r(r+r_2) + a^2)(2r+r_2) - 4Ma\xi - (2r-2M+r_2)(\eta + a^2 + \xi^2) = 0 \quad (\text{obtained from } \tilde{V}'(r) = 0). \quad (43)$$

From Eq. (43) we obtain two classes of solutions for  $\eta$  and  $\xi$ :

(1)

$$\eta = -\frac{r^2(r+r_2)^2}{a^2} \quad (44)$$

$$\xi = a + \frac{r(r+r_2)}{a} \quad (45)$$

(2)

$$\eta = \frac{-r^2[-8a^2M(2r+r_2) + ((r+r_2)(2r+r_2) - 2M(3r+r_2))^2]}{a^2(-2M+2r+r_2)^2} \quad (46)$$

$$\xi = \frac{a^2(2(M+r) + r_2) + r(r+r_2)(2r+r_2) - 2M(3r+r_2)}{a(2M-2r-r_2)}. \quad (47)$$

The first solution has  $\eta < 0$  which requires  $a^2 + |\eta| - \xi^2$  to be positive (see previous discussion). Substituting  $\eta$  and  $\xi$  from the first solution we note that  $a^2 + |\eta| - \xi^2 = -2r(r + r_2) < 0$  which makes the first solution unphysical and hence unacceptable. In the case of the second solution  $\eta$  may assume any sign depending on the value of  $r$ , and it can be shown that the suitable conditions as discussed earlier are satisfied. We will therefore work with the second solution.

### C. Equation of the critical curve

In this section we use the derived impact parameters from the last section to evaluate the celestial coordinates  $x$  and  $y$  of the critical curve as viewed by an observer at infinity. The position of the distant observer is taken to be

$(r_0, \theta_0)$  where we take  $r_0 \rightarrow \infty$  and  $\theta_0$  is the inclination angle of the observer. In order to obtain the outline of the critical curve in the observer's sky we consider the projection of the null geodesics onto the image plane.

In order to obtain the celestial coordinates we write the metric in terms of Bardeen tetrads [100–102], which are associated with observers to whom the black hole appears static:

$$e_{(t)}^\mu = \left( \sqrt{|g^{tt}|}, 0, 0, \frac{g^{t\phi}}{\sqrt{|g^{tt}|}} \right) \quad e_{(r)}^\mu = \sqrt{|g^{rr}|}(0, 1, 0, 0)$$

$$e_{(\theta)}^\mu = \sqrt{|g^{\theta\theta}|}(0, 0, 1, 0) \quad e_{(\phi)}^\mu = \left( 0, 0, 0, \sqrt{|g^{\phi\phi}| + \frac{(g^{t\phi})^2}{|g^{tt}|}} \right).$$

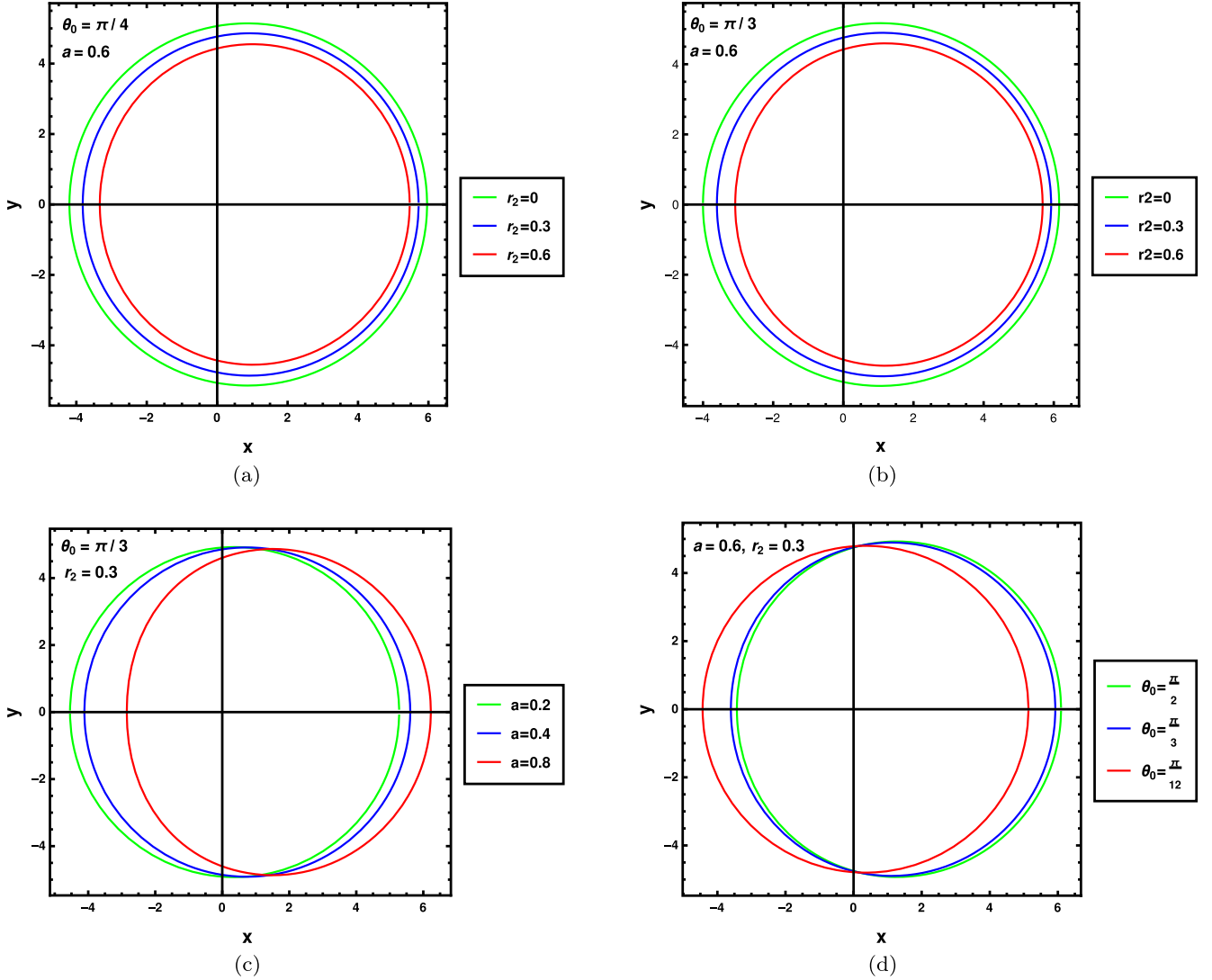


FIG. 1. (a) Change in the area enclosed by the critical curve with dilaton parameter  $r_2$ . We take the inclination angle to be  $\theta_0 = 45^\circ$  and the spin to be  $a = 0.6$ . (b) Change in the area enclosed by the critical curve with dilaton parameter  $r_2$ . We take the inclination angle to be  $\theta_0 = 60^\circ$  and the spin to be  $a = 0.6$ . (c) Change in the shape of the critical curve with spin-parameter  $a$ . We take the inclination angle as  $\theta_0 = 60^\circ$  and  $r_2 = 0.3$ . (d) Change in the shape of the critical curve with inclination angle  $\theta_0$ . Here we take the dilaton parameter  $r_2 = 0.3$  and spin  $a = 0.6$ . The above figure illustrates the variation in the structure of the critical curve with the dilaton parameter  $r_2$ , the spin parameter  $a$ , and the inclination angle  $\theta_0$ .

From the tetrads we can compute the components of four momentum  $p_{(i)} = e^j_{(i)} p_j$  of a locally inertial observer. The contravariant components of the four momentum  $p^{(k)} = \eta^{(k)(l)} p_{(l)}$  of the locally inertial observer are given as

$$p^{(t)} = \frac{E}{c} \left( c\sqrt{g^{tt}} - \xi \frac{g^{t\phi}}{\sqrt{g^{tt}}} \right) \quad p^{(r)} = \pm \sqrt{\frac{\mathcal{V}(r)}{\tilde{\rho}\Delta}}$$

$$p^{(\theta)} = \pm \sqrt{\frac{\Theta}{\tilde{\rho}}} \quad p^{(\phi)} = \sqrt{|g^{\phi\phi}| + \frac{(g^{t\phi})^2}{g^{tt}}} \xi.$$

A distant observer located at  $(r_0, \theta_0)$  will find the local apparent velocities of a photon to be  $v_{(\theta)} = \frac{p^{(\theta)}}{p^{(r)}}$  and  $v_{(\phi)} = \frac{p^{(\phi)}}{p^{(r)}}$  in which case the apparent perpendicular distance from the axis of rotation and the equatorial plane are respectively given by  $d_\phi = r_0 v_{(\phi)}$  and  $d_\theta = r_0 v_{(\theta)}$ . These are associated with the celestial coordinates  $x$  and  $y$  such that

$$x = \lim_{r_0 \rightarrow \infty} r_0 v_{(\phi)} = \lim_{r_0 \rightarrow \infty} \frac{r_0 p^{(\phi)}(r_0, \theta_0)}{p^{(r)}(r_0, \theta_0)} = -\frac{\xi}{\sin \theta_0} \quad (48)$$

$$y = \lim_{r_0 \rightarrow \infty} r_0 v_{(\theta)} = \lim_{r_0 \rightarrow \infty} \frac{r_0 p^{(\theta)}(r_0, \theta_0)}{p^{(r)}(r_0, \theta_0)} = \pm \sqrt{\Theta(\theta_0)}. \quad (49)$$

Figure 1 illustrates the variation in the shape and size of the critical curve with the dilaton parameter  $r_2$ , inclination angle  $\theta_0$ , and the black hole spin  $a$ . The figure reveals that the area enclosed by the critical curve decreases with an increase in the magnitude of the dilaton parameter  $r_2$ . We further note that when  $a$  and  $\theta_0$  are enhanced the critical curve becomes increasingly noncircular [103–106].

From the discussion presented in this section we note that the critical curve which represents the projection on sky of a particular set of null geodesics is a pure mathematical locus (depending solely on the background metric) and is not observable (the observable features which are closely related to the critical curve are the photon rings). The black hole shadow, on the other hand, refers to a flux depression at the center of a black hole image, and is an observable quantity. The structure of the observed black hole shadow depends not only on the background spacetime but is very strongly affected by the properties of the accretion flow around the compact object. The outer boundary of the observed shadow generally does not coincide with the critical curve except when the accretion is radially falling onto the black hole [107]. However, when the emission is dominated by matter orbiting in the equatorial plane, the shadow and the critical curve do not coincide [108]. Although the EHT Collaboration reports the angular diameter of the observed ring, they also mention the amount of offset that can be expected between the observed ring and the critical curve. Based on these data we compare our theoretical critical

curve with the observed images of M87\* and Sgr A\* which in turn enables us to establish constrains on the dilaton parameter  $r_2$ . We will discuss this in greater detail in the next section.

#### IV. COMPARISON WITH OBSERVATIONS AND CONTRAINS ON THE DILATON PARAMETER

In this section we aim to constrain the dilaton parameter  $r_2$  using the images of M87\* and SgrA\* released by the EHT Collaboration [7,13]. In order to obtain constrains on the dilaton parameter  $r_2$  we theoretically calculate the observables, namely, the angular diameter  $\Delta\theta$ , the axis ratio  $\Delta A$ , and the deviation from circularity  $\Delta C$  [109] for the critical curve, assuming the spacetime around the black hole to be described by the Kerr-Sen metric. In our approach, we use measurements for distance  $D$ , mass  $M$ , and the inclination angle  $\theta_0$  (angle between the line of sight and the jet axis) of the black hole determined from previous observations. The observables related to the critical curve which will be used to find the best estimate of the dilaton parameter  $r_2$  are discussed below.

*Angular diameter of the critical curve  $\Delta\theta$* : It is a measure of the angular width of the critical curve. If the maximum vertical width of the critical curve is  $\Delta y$  (also called the major axis length; see Fig. 2), the mass of the black hole is  $M$  and the distance of the black hole from the observer is  $D$  then the angular diameter of the critical curve  $\Delta\theta$  [109] is defined as

$$\Delta\theta = \frac{GM\Delta y}{c^2 D}. \quad (50)$$

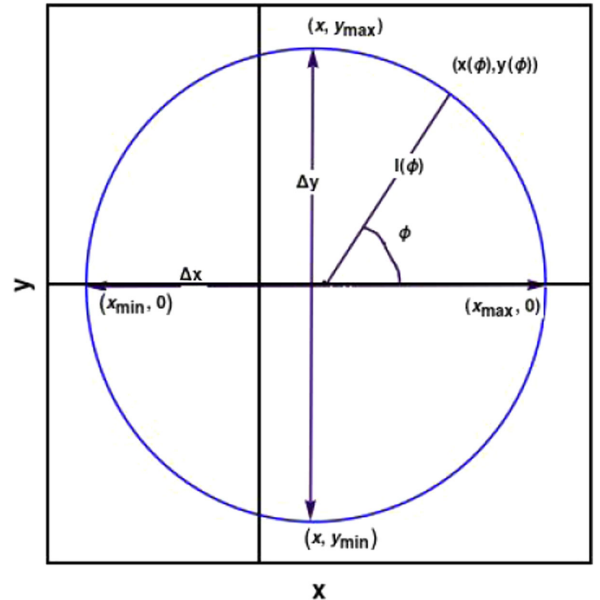


FIG. 2. Schematic diagram of the critical curve.

The value of  $\Delta y$  is calculated from the equation of the critical curve which contains the impact parameters  $\xi$  and  $\eta$ . The impact parameters in turn depend on  $r_2$ ,  $a$ , and the inclination angle  $\theta_0$ . Therefore, the angular diameter also depends on the three aforesaid parameters, and thus  $r_2$  can be constrained using EHT estimates of  $\Delta\theta$  assuming predetermined mass  $M$ , distance  $D$ , and inclination angle  $\theta_0$ .

*Axis ratio  $\Delta A$  of the black hole critical curve:* As the critical curve of the black hole is in general not circular, the major axis  $\Delta y$  and the minor axis  $\Delta x$  may not be equal. From Fig. 2, the axis ratio  $\Delta A$  is defined as [109]

$$\Delta A = \frac{\Delta y}{\Delta x}, \quad (51)$$

where the minor axis  $\Delta x$  is also calculated from the equation of the critical curve, and hence,  $\Delta A$  also depends on  $r_2$ ,  $a$  and  $\theta_0$ .

*Deviation from Circularity  $\Delta C$ :* Deviation from circularity  $\Delta C$  measures the amount of deviation from the circular shape of the critical curve [109]. It is defined as follows:

$$\Delta C = \frac{1}{R_{\text{avg}}} \sqrt{\frac{1}{2\pi} \int_0^{2\pi} \{l(\phi) - R_{\text{avg}}\}^2 d\phi} \quad (52)$$

$$\text{Here, } R_{\text{avg}} = \sqrt{\frac{1}{2\pi} \int_0^{2\pi} l(\phi)^2 d\phi} \quad (53)$$

$$l(\phi) = \sqrt{(x(\phi) - x_c)^2 + y(\phi)^2}. \quad (54)$$

In the above expression  $R_{\text{avg}}$  is the average radius of the critical curve.  $l(\phi)$  is the length of the line joining the point  $(x(\phi), y(\phi))$  on the critical curve and the geometric center  $(x_c, 0)$  (see Fig. 2). It must be noted that due to reflection symmetry of the Kerr-Sen metric, the shape of the critical curve is symmetric about the  $x$  axis; hence the  $y$  coordinate of the geometric center is 0. The  $x$  coordinate of the geometric center is calculated using

$$x_c = \frac{\int_0^{2\pi} x(\phi) dS}{\int_0^{2\pi} dS} \quad (\text{here } dS \text{ is the area element}). \quad (55)$$

*EHT observations of M87\*:* The EHT Collaboration measured the angular diameter  $\Delta\theta$ , the axis ratio  $\Delta A$ , and the deviation from circularity  $\Delta C$  for the observed ring of M87\*, the supermassive black hole candidate at the center of the galaxy M87 [7–9]. The values reported are given below.

- (1)  $\Delta\theta = (42 \pm 3) \mu\text{as}$ . The EHT also reports a maximum offset of 10% between the angular diameter of the observed primary ring and the critical curve. Thus, the critical curve angular diameter can be as small as  $\Delta\theta = (37.8 \pm 3) \mu\text{as}$  [7–9].

- (2)  $\Delta A \lesssim 4/3$  [7–9].

- (3)  $\Delta C \lesssim 10\%$  [7–9].

In order to determine the observationally favored dilaton parameter  $r_2$ , we theoretically derive the above three observables as functions of the parameters  $r_2$ ,  $a$ , and  $\theta_0$ . As evident from Eq. (50) a theoretical computation of the angular diameter  $\Delta\theta$  requires independent measurements of the black hole mass, distance, and inclination angle (required to derive  $\Delta y$ ). We use previously estimated masses and distance of this source to compute the theoretical angular diameter. The distance of M87\* as reported from stellar population measurements turns out to be  $D = (16.8 \pm 0.8) \text{ Mpc}$  [110–112]. The angle of inclination, which is the angle between the line of sight and the jet axis (the jet axis is believed to coincide with the spin axis of the black hole) is  $(17 \pm 2)^\circ$  [113]. The mass of M87\* has been measured using different methods. The mass measurement by modeling surface brightness and dispersion in stellar velocity was found to be  $M = 6.2_{-0.6}^{+1.1} \times 10^9 M_\odot$  [8,114,115]. Mass measurements from the kinematic study of the gas disk gives  $M = 3.5_{-0.3}^{+0.9} \times 10^9 M_\odot$  [8,116]. Mass measured from the image of M87\* by the EHT Collaboration assuming general relativity turns out to be  $M = (6.5 \pm 0.7) \times 10^9 M_\odot$  [7–9].

*EHT observations of Sgr A\*:* In May 2022, the EHT Collaboration released the image of the black hole Sgr A\* present at the Galactic Center of the Milky Way Galaxy. The angular diameter of the primary ring is found to be  $\Delta\theta = (51.8 \pm 2.3) \mu\text{as}$  [13–18]. The angular diameter of the critical curve inferred from the observed primary ring is  $\Delta\theta = (48.7 \pm 7) \mu\text{as}$  [13].

The mass and distance of Sgr A\* reported by the Keck Collaboration keeping the redshift parameter free, are  $M = (3.975 \pm 0.058 \pm 0.026) \times 10^6 M_\odot$  [117] and  $D = (7959 \pm 59 \pm 32) \text{ pc}$  [117] respectively. Fixing the value of the redshift parameter to unity, the mass and distance of Sgr A\* reported by the Keck team are  $M = (3.951 \pm 0.047) \times 10^6 M_\odot$  and  $D = (7935 \pm 50) \text{ pc}$ . The mass and distance of Sgr A\* reported by the GRAVITY Collaboration are  $M = (4.261 \pm 0.012) \times 10^6 M_\odot$  and  $D = (8246.7 \pm 9.3) \text{ pc}$  [118,119] respectively. When systematics due to optical aberrations are taken into account, the GRAVITY Collaboration constrains the mass and distance of Sgr A\* to  $M = (4.297 \pm 0.012 \pm 0.040) \times 10^6 M_\odot$  and  $D = (8277 \pm 9 \pm 33) \text{ pc}$  respectively. Apart from mass and distance we also need to provide independent measurements of the inclination angle to establish observational constraints on  $r_2$ . From [120] we take  $\theta_0 \simeq 134^\circ$  (or equivalently  $46^\circ$ ). When models based on extensive numerical simulations are compared with the observed image of Sgr A\*, one concludes that the inclination angle of the source is  $\theta_0 < 50^\circ$ . The estimates for the axis ratio ( $\Delta A$ ) and the deviation from circularity  $\Delta C$  for the image of Sgr A\* by the EHT Collaboration are yet to be



released; hence, for Sgr A\* the angular diameter  $\Delta\theta$  will only be used for estimating constraints on  $r_2$ .

To constrain the Kerr-Sen/dilaton parameter  $r_2$  using the EHT estimates for the critical curve, we proceed with the following approach:

- (1) We derive the outline of the critical curve by calculating the impact parameters  $\xi$  and  $\eta$  for the Kerr-Sen black hole. We obtain the parametric equations of the black hole critical curve outline.
- (2) We fix the value of  $r_2$  and vary the spin  $a$  of the black hole in a suitable range such that the event horizon radius is real and positive.
- (3) For each combination of  $(r_2, a)$  we calculate the values of angular diameter  $\Delta\theta$ , axis ratio  $\Delta A$ , and the deviation from circularity  $\Delta C$ . In these calculations we use values of mass  $M$ , distance  $D$ , and inclination angle  $\theta_0$  from previous measurements as discussed above.
- (4) Then we repeat steps 2 and 3 for different values of  $r_2$  up to  $r_2 = 1.8$ . It must be noted that the dilaton parameter  $r_2$  varies in the range  $0 \leq r_2 \leq 2$  since the horizon radius (in units of  $M$ ) is given by  $r_h = 1 - \frac{r_2}{2} + \sqrt{(1 - \frac{r_2}{2})^2 - a^2}$  which needs to be real and positive.
- (5) After obtaining values for  $\Delta\theta$ ,  $\Delta A$ , and  $\Delta C$  we plot contour plots for the angular diameter  $\Delta\theta$ , density plots for the axis ratio  $\Delta A$ , and the deviation from circularity  $\Delta C$  as functions of  $r_2$  and  $a$ .
- (6) The values of  $r_2$  which are able to reproduce the EHT estimated  $\Delta\theta$ ,  $\Delta A$ , and  $\Delta C$  for the critical curve give us the allowed values of  $r_2$  based on the EHT data.

At this point we emphasize once again that the critical curve we have computed theoretically cannot be directly compared to the observed images of M87\* and Sgr A\* reported by the EHT Collaboration. This is because the critical curve is not an observable quantity. It is associated with the projection on sky of a particular set of null geodesics and depends only on the background metric and the inclination angle. The outline of the observed image on the other hand depends both on the background spacetime as well as the properties of the accretion flow. For M87\*, the observed ring and the critical curve exhibit a maximum offset of 10% [121]. The angular diameter of the observed ring of M87\* as reported by the EHT Collaboration is  $\Delta\theta = (42 \pm 3) \mu\text{as}$ . With 10% maximum offset, the angular diameter of the critical curve can be as small as  $\Delta\theta = (37.8 \pm 3) \mu\text{as}$ . In what follows, we will use the angular diameter of the critical curve to derive the magnitude of  $r_2$  which is observationally favored.

For Sgr A\*, the emission ring has an angular diameter of  $\Delta\theta = (51.8 \pm 2.3) \mu\text{as}$  [13–18]. The EHT papers define a ratio  $\alpha_1 = d_m/d_{sh}$  [18] where  $d_m$  is the diameter of the

observed emission ring and  $d_{sh}$  is the diameter of the critical curve. Note that in the EHT papers [13–18], the critical curve is referred as the shadow (we follow here the terminology mentioned in Gralla *et al.* [93]). While the diameter of the emission ring is observationally derived, the magnitude of  $\alpha_1$  is obtained from a library of simulations assuming various accretion models (see Fig. 7 of [18]). Thus, the diameter of the critical curve depends on the observed diameter of the emission ring and on  $\alpha_1$  which is model dependent. From Fig. 7 of [18] one can note that the offset between the observed ring diameter and the critical curve diameter varies for different models. Further, note that, it is not unlikely that other models (e.g., radially infalling models, other assumptions regarding the electron heating prescription, general relativistic magnetohydrodynamics (GRMHD) flows starting from an initial condition that differs from standard analytical tori) not included in the simulation library would lead to other values of  $\alpha_1$ . This however is beyond the scope of this work. Considering an average over all models, the EHT Collaboration reports the critical curve angular diameter to be  $\Delta\theta = (48.7 \pm 7) \mu\text{as}$  (Table 1 of [13]). In the following discussion we will report the observationally preferred magnitude of  $r_2$  from the image of Sgr A\*, based on the critical curve diameter reported by the EHT, i.e.,  $\Delta\theta = (48.7 \pm 7) \mu\text{as}$  [13].

As discussed earlier, theoretical estimation of the critical curve angular diameter requires independent measurement of mass, distance, and inclination angle of the source [see Eq. (50)]. Although these three quantities have been estimated for Sgr A\* and M87\*, they have their associated error bars. We therefore need to take these error bars into account while calculating the theoretical angular diameter. Consider the mass of the source to be  $M_{-\Delta M_2}^{+\Delta M_1}$ , distance of the source to be  $D_{-\Delta D_2}^{+\Delta D_1}$ , and the inclination angle to be  $\theta_0 \pm \Delta\theta_0$ . In the above discussion we have mentioned these quantities for Sgr A\* and M87\*. Since the theoretical angular diameter is directly proportional to the mass and inversely proportional to the distance [Eq. (50)], the angular diameter calculated with maximum mass ( $M = M + \Delta M_1$ ) and minimum distance ( $D = D - \Delta D_2$ ) when compared with observations will give the maximum allowed magnitude of  $r_2$ . Similarly, when the theoretical angular diameter calculated with minimum mass ( $M = M - \Delta M_2$ ) and maximum distance ( $D = D + \Delta D_1$ ) is compared with observations, the minimum allowed magnitude of  $r_2$  can be derived. Thus, for every combination of mass and distance measurement for M87\* and Sgr A\* we consider three scenarios, namely, theoretical angular diameter calculated with (i) the minimum mass and maximum distance, (ii) the central value of mass and distance, and (iii) the maximum mass and minimum distance. Also note that the theoretical angular diameter depends on the inclination angle which has its associated error bar. The error in  $\theta_0$  also affects the constraints on  $r_2$ . The  $\theta_0$  for M87\* and SgrA\* are  $(17 \pm 2)^\circ$  [113] and  $(133.911 \pm 0.052)^\circ$

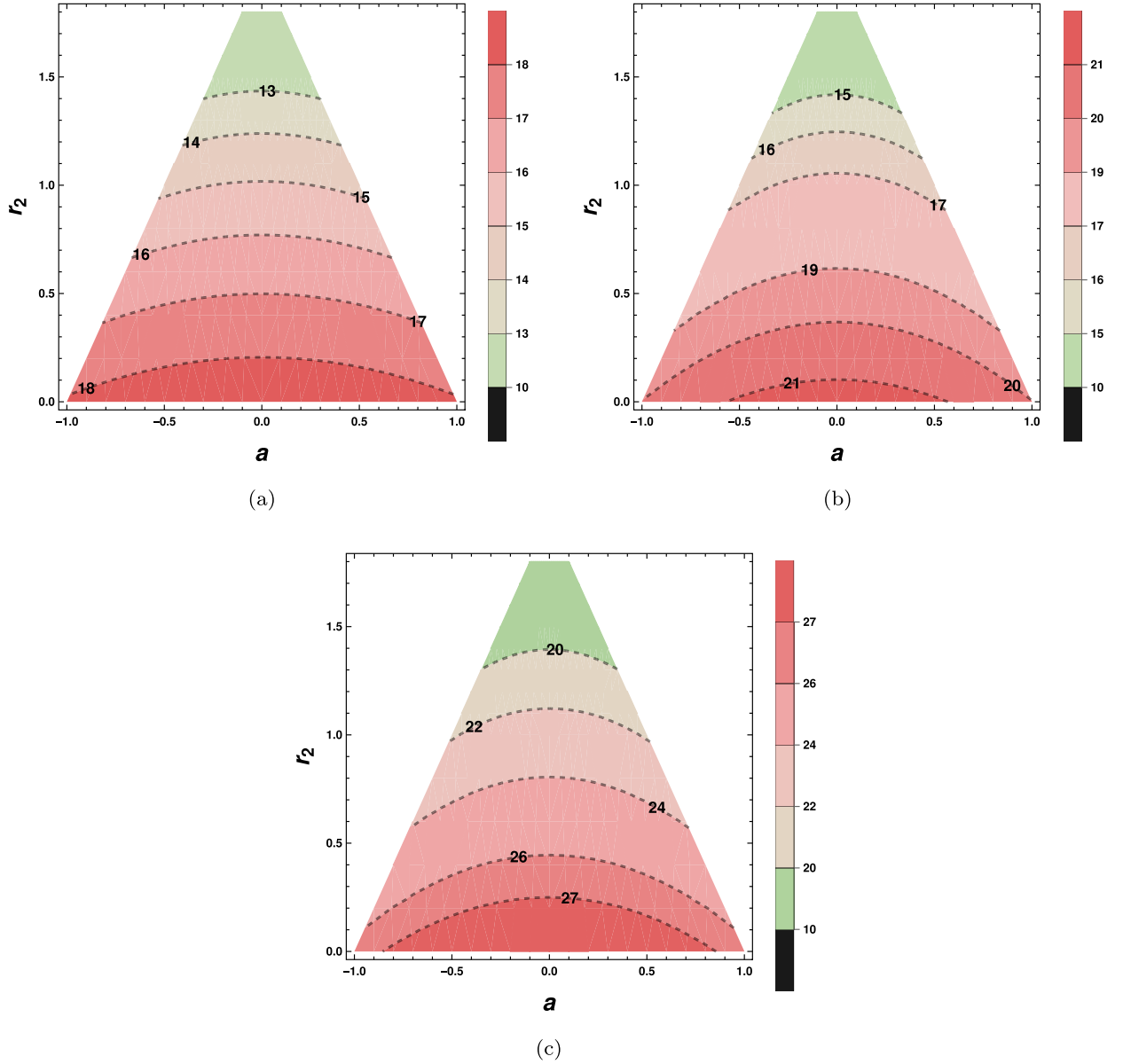


FIG. 3. The figure illustrates the variation of the angular diameter of M87\* with metric parameters  $r_2$  and  $a$  for  $M = 3.5^{+0.9}_{-0.3} \times 10^9 M_\odot$  and distance  $D = 16.8 \pm 0.8$  Mpc. In order to compute the angular diameter the inclination angle is taken to be  $\theta_0 = 17^\circ$ . (a) Variation of angular diameter of M87\* (calculated with minimum mass  $M = 3.2 \times 10^9 M_\odot$  and maximum distance  $D = 17.6$  Mpc) with  $r_2$  and  $a$ . (b) Variation of angular diameter of M87\* (calculated with central value of mass  $M = 3.5 \times 10^9 M_\odot$  and distance  $D = 16.8$  Mpc) with  $r_2$  and  $a$ . (c) Variation of angular diameter of M87\* (calculated with maximum mass  $M = 4.4 \times 10^9 M_\odot$  and minimum distance  $D = 16$  Mpc) with  $r_2$  and  $a$ .

(equivalent to  $(46.089 \pm 0.052)^\circ$  [120], respectively). The errors in  $\theta_0$  are small compared to the central values, and hence they do not drastically affect the constraints on  $r_2$ . Furthermore, from Fig. 1(d) one may note that the features of critical curve do not change appreciably for variation in  $\theta_0$  from  $\pi/3$  to  $\pi/2$ . Thus, only large variations in  $\theta_0$  can change the critical curve appreciably, e.g.,  $\pi/12$  to  $\pi/3$ . Hence, we keep the value of the inclination angle fixed to the central value in our analysis.

Constraints on the dilaton parameter  $r_2$  from EHT observations of M87\*: Here we discuss the constraints on the dilaton parameter  $r_2$  based on the critical curve angular diameter ( $(37.8 \pm 3) \mu\text{as}$ ) derived from the observed ring of M87\* by the EHT Collaboration. In order to get an understanding of the allowed values of  $r_2$ , we theoretically compute the observables, namely,  $\Delta\theta$  (angular diameter),  $\Delta A$  (axis ratio), and  $\Delta C$  (deviation from circularity) related to the black hole critical curve, which have been discussed

toward the beginning of this section. It is important to recall that these observables depend on the metric parameters  $r_2$ ,  $a$ , and the inclination angle  $\theta_0$ . We use previously estimated values of the inclination angle  $\theta_0 = (17 \pm 2)^\circ$  [113] for calculating the theoretical angular diameter. Since the error bar in the inclination angle is small, we will use the central value  $\theta_0 = 17^\circ$  throughout our analysis (see discussion above). In addition, the theoretically derived  $\Delta\theta$  requires independent estimates of the mass  $M$  and the distance  $D$  of the black hole [see Eq. (50)]. Based on stellar population

measurements, the distance of M87\* is estimated to be  $D = (16.8 \pm 0.8)$  Mpc [110–112], which will be considered along with error bars in our analysis. The mass of M87\* has been independently estimated based on stellar dynamics and gas dynamics studies. We first consider constrains on  $r_2$  assuming a mass of M87\* based on gas dynamics studies, i.e.,  $M = 3.5_{-0.3}^{+0.9} \times 10^9 M_\odot$  (see Fig. 3). To obtain the maximum allowed range of  $r_2$  we calculate the theoretical angular diameter of the critical curve assuming

- (1) (minimum mass, maximum distance)  $\rightarrow (M = 3.2 \times 10^9 M_\odot, D = 17.6$  Mpc [Fig. 3(a)]).
- (2) (central mass, central distance)  $\rightarrow (M = 3.5 \times 10^9 M_\odot, D = 16.8$  Mpc [Fig. 3(b)]).
- (3) (maximum mass, minimum distance)  $\rightarrow (M = 4.4 \times 10^9 M_\odot, D = 16$  Mpc [Fig. 3(c)]).

In Fig. 3 the contour plots for variation of angular diameter of the critical curve with the dilaton parameter  $r_2$  and spin  $a$  (when mass measurement from gas dynamics is considered) are shown. In all the subfigures of Fig. 3 we note that there is no suitable  $r_2$  in the range 0 to 2 (obtained from the considerations of a real, positive event horizon) which can reproduce the inferred critical curve angular diameter of M87\* with 10% maximum offset (i.e.,  $\Delta\theta = 37.8 \pm 3 \mu\text{as}$ ). Thus, when gas dynamics mass measurements for M87\* are considered, the EHT estimated angular diameter cannot be explained for any value of the

dilaton parameter  $r_2$ , i.e., we do not obtain any constrains on  $r_2$  in this case. The low values of theoretical angular diameters in Fig. 3 are because of the low magnitude of mass reported from gas dynamics studies. Hence, it seems that the mass of M87\* estimated from gas dynamics measurements needs to be revisited.

We now consider calculating the theoretical angular diameter of the critical curve assuming mass of M87\* based on stellar dynamics measurements, i.e.,  $M = 6.2_{-0.6}^{+1.1} \times 10^9 M_\odot$ . Once again, in order to obtain the maximum observationally allowed range of  $r_2$  we consider

- (1) (minimum mass, maximum distance)  $\rightarrow (M = 5.6 \times 10^9 M_\odot, D = 17.6$  Mpc [Fig. 4(a)]).
- (2) (central mass, central distance)  $\rightarrow (M = 6.2 \times 10^9 M_\odot, D = 16.8$  Mpc [Fig. 4(b)]).
- (3) (maximum mass, minimum distance)  $\rightarrow (M = 7.3 \times 10^9 M_\odot, D = 16$  Mpc [Fig. 4(c)]).

In Fig. 4 we present contour plots for the variation of critical curve angular diameter with dilaton parameter  $r_2$  and  $a$  for the above three combinations of mass and distance. We note from Fig. 4(a) that with minimum mass ( $M = 5.6 \times 10^9 M_\odot$ ) and maximum distance ( $D = 17.6$  Mpc), there is no value of  $r_2$  that can explain the EHT estimated angular diameter  $\Delta\theta = 37.8 \pm 3 \mu\text{as}$ . When the central value of mass  $M = 6.2 \times 10^9 M_\odot$  and distance  $D = 16.8$  Mpc are considered [Fig. 4(b)],  $r_2 \simeq 0$  best explains the central value of the EHT inferred angular diameter (i.e.,  $\Delta\theta = 37.8 \mu\text{as}$ ), marked by the red solid line in Fig. 4(b) while  $0.1 \lesssim r_2 \lesssim 0.4$  is required to explain the angular diameter within the lower  $1-\sigma$  interval (i.e.,  $\Delta\theta = 37.8 - 3 = 34.8 \mu\text{as}$ ). This is marked by the red dashed line in Fig. 4(b). Finally, when maximum mass ( $M = 7.3 \times 10^9 M_\odot$ ) and minimum distance ( $D = 16$  Mpc) are used to calculate the theoretical angular diameter,  $0.8 \lesssim r_2 \lesssim 1$  is required to reproduce the central value of the EHT

estimated angular diameter (i.e.,  $\Delta\theta = 37.8 \mu\text{as}$ ) marked by the red solid line in Fig. 4(c). When the  $1-\sigma$  interval in the angular diameter is considered (i.e.,  $\Delta\theta = 37.8 \pm 3 \mu\text{as}$ ), the range of  $r_2$  turns out to be  $0.5 \lesssim r_2 \lesssim 1.2$  [see red dashed lines in Fig. 4(c)]. The above discussion elucidates that the image of M87\* exhibits a preference toward the Kerr scenario (since, with central values of mass and distance, the central value of the EHT estimated critical curve angular diameter, can be best explained by  $r_2 \simeq 0$ ). However, non-zero dilaton charge is also allowed when errors in mass and distance are taken into account or the  $1-\sigma$  interval in the derived critical curve angular diameter is considered. Thus, the image of M87\* does not reject the Kerr-Sen scenario.

For completeness we also calculate the theoretical angular diameter with mass  $M \simeq 6.5 \times 10^9 M_\odot$  which is the mass derived by the EHT Collaboration from the observed ring of M87\* assuming general relativity. Since this is the largest among all the three masses (when

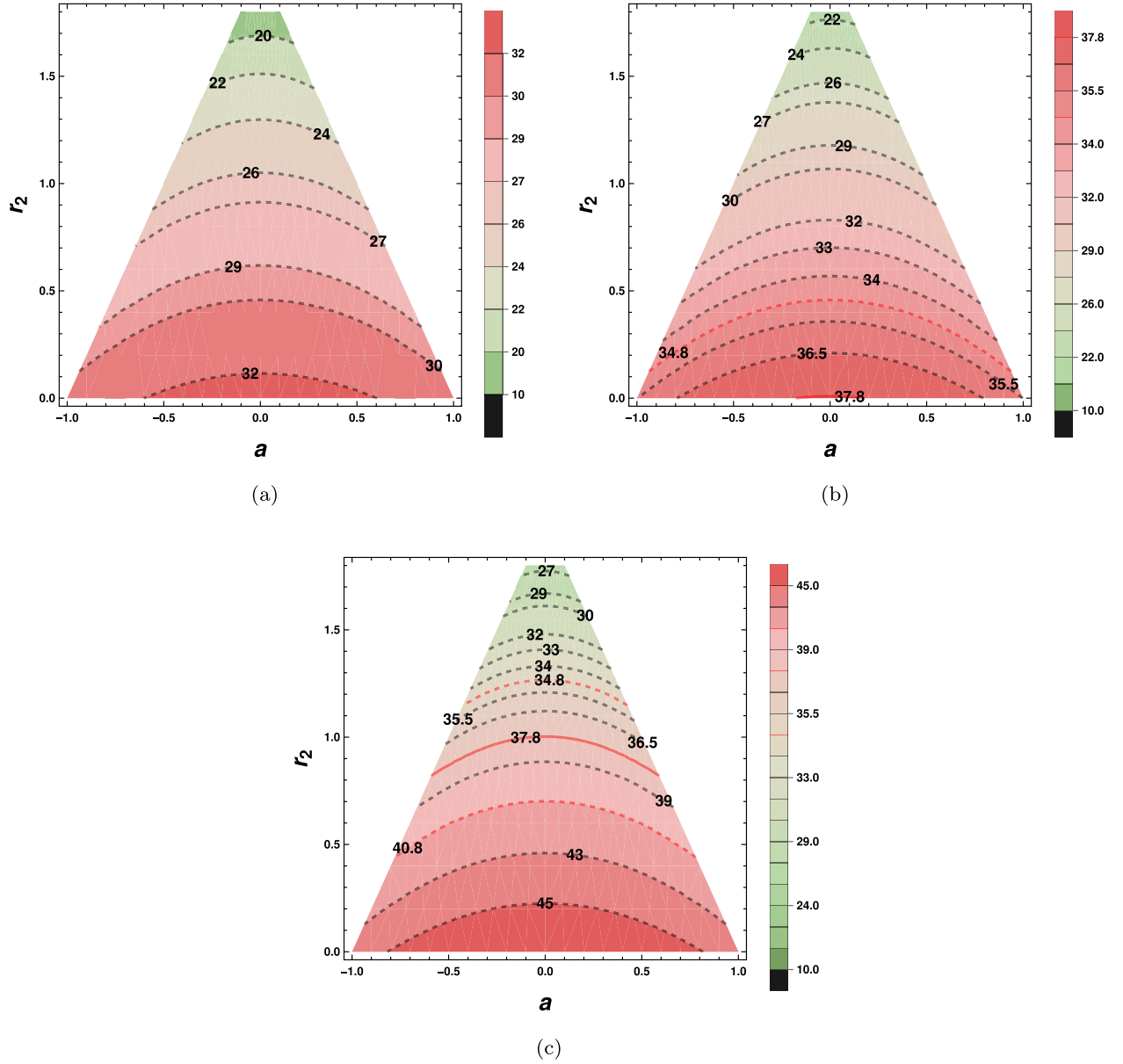


FIG. 4. (a) Contour plots for critical curve angular diameter of M87\* for different  $r_2$  and  $a$  assuming minimum mass  $M = 5.6 \times 10^9 M_\odot$  and maximum distance  $D = 17.6$  Mpc. (b) Contour plots for critical curve angular diameter of M87\* for different  $r_2$  and  $a$  assuming central value of mass  $M = 6.2 \times 10^9 M_\odot$  and distance  $D = 16.8$  Mpc. (c) Contour plots for critical curve angular diameter of M87\* for different  $r_2$  and  $a$  assuming maximum mass  $M = 7.3 \times 10^9 M_\odot$  and minimum distance  $D = 16$  Mpc. The figure illustrates the variation of the critical curve angular diameter for M87\* with metric parameters  $r_2$  and  $a$  for  $M = 6.2^{+1.1}_{-0.6} \times 10^9 M_\odot$  and distance  $D = 16.8 \pm 0.8$  Mpc. In order to compute the angular diameter, the inclination angle is taken to be  $\theta_0 = 17^\circ$ . The red solid contours represent the central value of the EHT inferred critical curve angular diameter, and the red dashed contours represent the corresponding  $1-\sigma$  interval values.

the central values are considered), it can explain the derived critical curve angular diameter of  $\Delta\theta = 37.8 \mu\text{as}$  (denoted by the red solid line in Fig. 5) for  $0 \lesssim r_2 \lesssim 0.2$ . When the lower  $1-\sigma$  interval is considered higher values of  $r_2$  are allowed, viz.,  $0.4 \lesssim r_2 \lesssim 0.6$  (denoted by the red dashed line in Fig. 5). However,  $M \simeq 6.5 \times 10^9 M_\odot$  should not be used to infer the observationally favored magnitude of  $r_2$  since this mass is derived from the observed image

diameter assuming GR. Therefore, using this mass estimate we cannot constrain another alternative gravity theory.

We now discuss the constrains on  $r_2$  from the other two observables  $\Delta C$  and  $\Delta A$ . The theoretical computation of these two observables does not require information about the mass and distance of the source. One however needs to provide the inclination angle of the source (which in the present case is  $17^\circ$ ) to obtain  $\Delta C$  and  $\Delta A$  as functions of  $r_2$

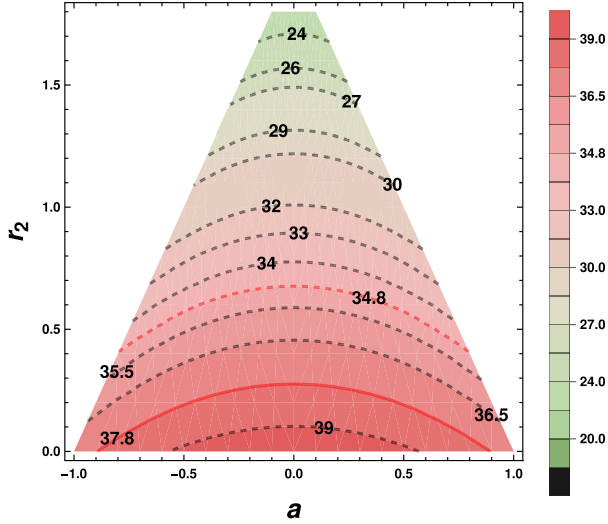


FIG. 5. The above figure demonstrates the dependence of the angular diameter of the critical curve of M87\* on the dilaton parameter  $r_2$  and the spin parameter  $a$  assuming distance  $D \simeq 16.8$  Mpc and mass  $M \simeq 6.5 \times 10^9 M_\odot$ . This mass is derived by the EHT team from the observed image assuming GR. Therefore, we cannot use this mass to constrain parameters of another alternate gravity theory. The contours with  $M \simeq 6.5 \times 10^9 M_\odot$  are plotted for the purpose of comparison and completeness only.

and  $a$ . According to the EHT results, the deviation from circularity  $\Delta C \lesssim 10\%$  [7–9] or 0.1 for M87\*. The density plot of  $\Delta C$  for M87\* is shown in Fig. 6(a).

From the density plot we observe that for all values of spin and  $r_2$ ,  $\Delta C < 10\%$  or 0.1 is realized. Thus, the  $\Delta C$  estimate for M87\* does not give any additional bound on the dilaton parameter  $r_2$ . The EHT Collaboration estimates

an upper bound on the axis ratio  $\Delta A$  for the image of M87\*, i.e.,  $\Delta A < \frac{4}{3}$  [7–9]. The density plot for the axis ratio  $\Delta A$  in Fig. 6(b) indicates that for all values of  $r_2$  and  $a$  the axis ratio  $\Delta A < \frac{4}{3}$ . Thus, the EHT estimate of the axis ratio  $\Delta A$  for M87\* does not provide any additional constrain on the dilaton parameter  $r_2$ . It can be said that the axis ratio estimate allows nonzero values of the dilaton parameter, although it does not strictly constrain it.

*Constrains on the dilaton parameter  $r_2$  from EHT observations of Sgr A\*:* The EHT Collaboration measured the angular diameter of the observed ring of Sgr A\* to be  $\Delta\theta = (51.8 \pm 2.3) \mu\text{as}$  [13–18]. The critical curve angular diameter derived from the observed ring is estimated to be  $\Delta\theta = (48.7 \pm 7) \mu\text{as}$  [13]. From the previous discussion we may recall that the critical curve angular diameter is offset from the angular diameter of the primary ring by a factor of  $\alpha_1 = \frac{d_m}{d_{sh}}$  obtained from a library of simulations assuming various accretion models [18]. The critical curve angular diameter is thus model dependent. It turns out that “the envelope of the 68<sup>th</sup> percentile credible intervals across the different methods span[s] 41.7 – 55.6  $\mu\text{as}$ ” [18]. Therefore, the model averaged estimate of  $d_{sh}$  for Sgr A\* is  $(55.6 + 41.7)/2 \pm (55.6 - 41.7)/2 \simeq 48.7 \pm 7 \mu\text{as}$  which is quoted in Table 1 of [13]. We will constrain the dilaton parameter  $r_2$  based on the angular diameter of the critical curve, i.e.,  $\Delta\theta = (48.7 \pm 7) \mu\text{as}$ .

The theoretical angular diameter depends on the mass  $M$ , the distance  $D$ , the inclination angle  $\theta_0$ , and the metric parameters  $r_2$  and  $a$  [see Eq. (50)]. As before, we use previously measured masses and distances of the source to compute the theoretical angular diameter which is then compared with the EHT estimates to establish constrains on

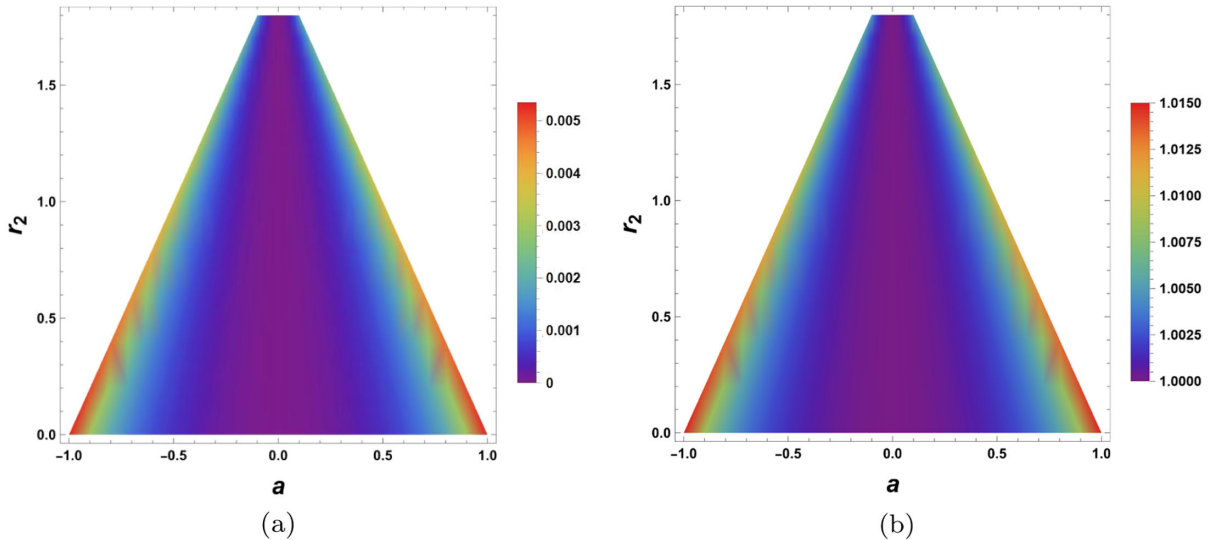


FIG. 6. (a) Figure illustrating the dependence of the deviation from circularity  $\Delta C$  on  $r_2$  and  $a$ . Here  $\Delta C$  has been calculated assuming the inclination angle  $\theta_0 = 17^\circ$  corresponding to M87\*. (b) Figure illustrating the dependence of the axis ratio  $\Delta A$  on  $r_2$  and  $a$ . Here  $\Delta A$  has been calculated assuming the inclination angle  $\theta_0 = 17^\circ$  corresponding to M87\*. The above figure depicts the variation of  $\Delta C$  and  $\Delta A$  for M87\* with the dilaton parameter  $r_2$  and the spin parameter  $a$ .

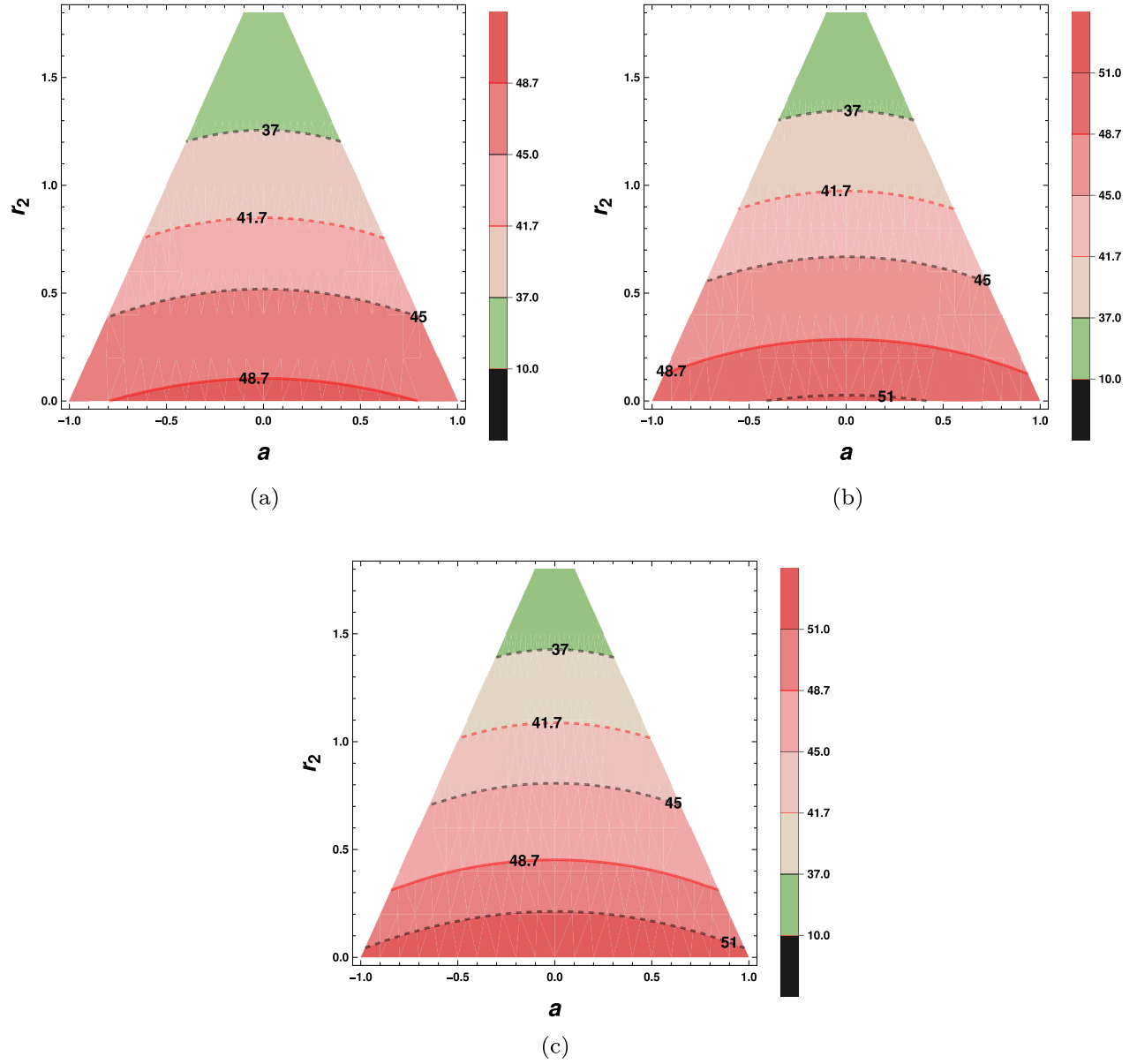


FIG. 7. (a) The above figure demonstrates the variation of the critical curve angular diameter of Sgr A\* with  $r_2$  and  $a$  assuming minimum mass  $M = 3.891 \times 10^6 M_\odot$  and maximum distance  $D = 8.050$  kpc. (b) The above figure demonstrates the variation of the critical curve angular diameter of Sgr A\* with  $r_2$  and  $a$  assuming central value of mass  $M = 3.975 \times 10^6 M_\odot$  and distance  $D = 7.959$  kpc. (c) The above figure demonstrates the variation of the critical curve angular diameter of Sgr A\* with  $r_2$  and  $a$  assuming maximum mass  $M = 4.059 \times 10^6 M_\odot$  and minimum distance  $D = 7.868$  kpc. Contour plots for angular diameter of critical curve of Sgr A\* assuming  $M = (3.975 \pm 0.058 \pm 0.026) \times 10^6 M_\odot$  and  $D = (7959 \pm 59 \pm 32)$  pc. In order to compute the angular diameter the inclination angle is taken to be  $\theta_0 = 46^\circ$ . The critical curve angular diameter ( $\Delta\theta = 48.7 \pm 7 \mu\text{as}$ ) inferred by the EHT team is represented by the red contour lines (the red solid line corresponds to the central value while the  $1\text{-}\sigma$  contours are represented by the red dashed lines).

$r_2$ . We also take into account the effect of errors in mass and distance of Sgr A\* in determining constraints on the dilaton parameter  $r_2$ . The angle of inclination has an estimated upper bound  $\theta_0 < 50^\circ$  obtained by comparing the image of Sgr A\* with extensive numerical simulations [13]. Following [120] we fix the inclination angle to be  $\theta_0 = 46^\circ$  in our present work.

In Figs. 7–10 the angular diameter  $\Delta\theta$  of the critical curve for Sgr A\* is plotted for different estimates of mass and distance. The mass and distance of the source have been well constrained by the Keck team and the GRAVITY Collaboration. We first discuss the constraints on  $r_2$  assuming distance and mass measurements by the Keck team [117]:

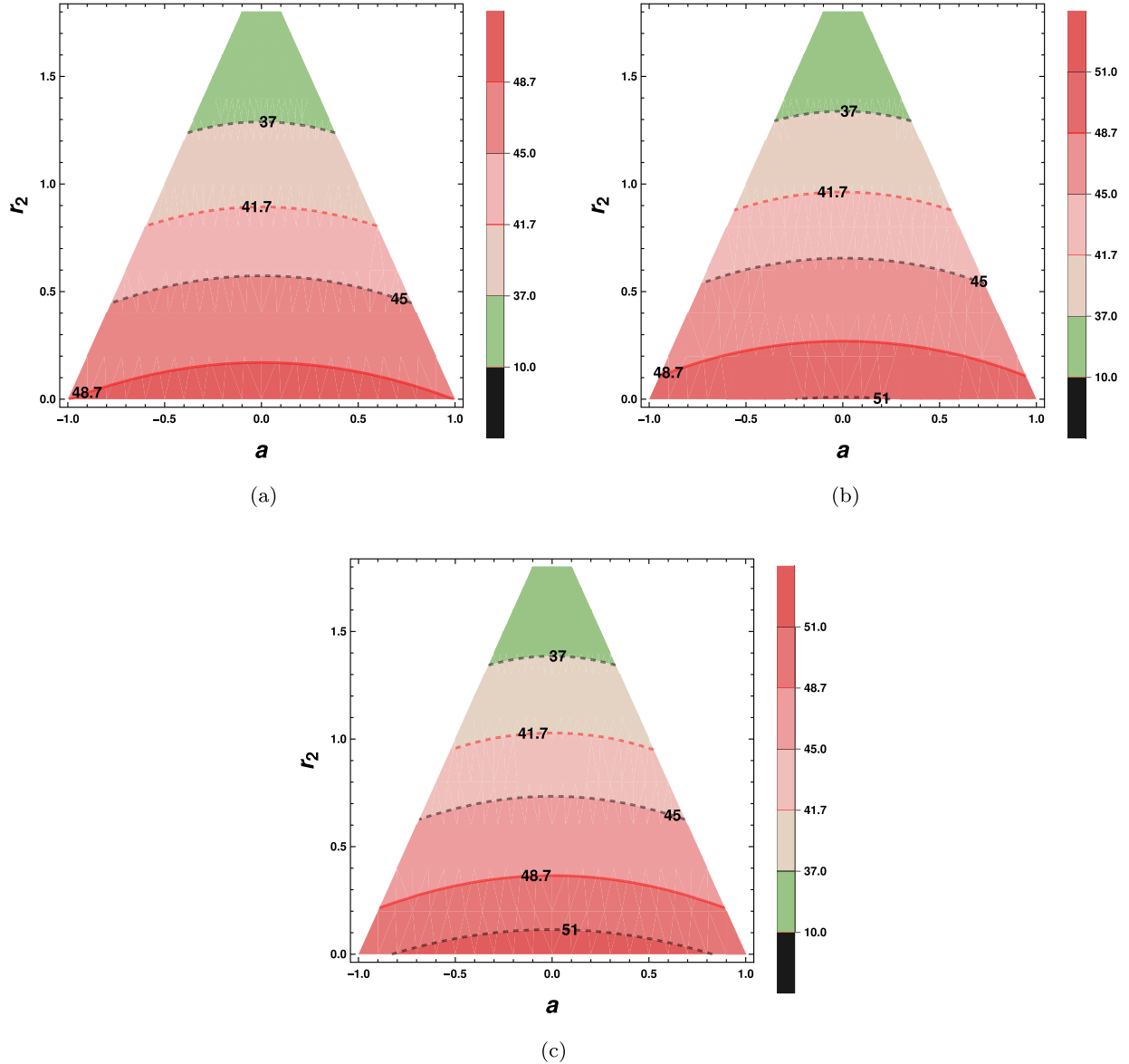


FIG. 8. (a) The above figure demonstrates the variation of critical curve angular diameter of Sgr A\* with  $r_2$  and  $a$  assuming  $M = 3.904 \times 10^6 M_\odot$  and  $D = 7.985$  kpc. (b) The above figure demonstrates the variation of critical curve angular diameter of Sgr A\* with  $r_2$  and  $a$  assuming  $M = 3.951 \times 10^6 M_\odot$  and  $D = 7.935$  kpc. (c) The above figure demonstrates the variation of critical curve angular diameter of Sgr A\* with  $r_2$  and  $a$  assuming  $M = 3.998 \times 10^6 M_\odot$  and  $D = 7.885$  kpc. Contour plots for critical curve angular diameter for Sgr A\* assuming  $M = (3.951 \pm 0.047) \times 10^6 M_\odot$  and  $D = (7935 \pm 50)$  pc. In order to compute the angular diameter the inclination angle is taken to be  $\theta_0 = 46^\circ$ . The critical curve angular diameter ( $\Delta\theta = 48.7 \pm 7 \mu\text{as}$ ) inferred by the EHT team is represented by the red contour lines (the red solid line corresponds to the central value while the  $1\text{-}\sigma$  contours are represented by the red dashed lines).

(1) Keeping the red-shift parameter free the Keck team reports the mass and distance of Sgr A\* to be  $M = (3.975 \pm 0.058 \pm 0.026) \times 10^6 M_\odot$  and  $D = (7959 \pm 59 \pm 32)$  pc, respectively. We take into account the error in mass and distance in our present analysis. To derive the maximum allowed range of  $r_2$  we calculate the theoretical angular diameter of the critical curve with

- (i) (minimum mass, maximum distance)  $\rightarrow (M = 3.891 \times 10^6 M_\odot, D = 8.050$  kpc [Fig. 7(a)]).
- (ii) (central mass, central distance)  $\rightarrow (M = 3.975 \times 10^6 M_\odot, D = 7.959$  kpc [Fig. 7(b)]).
- (iii) (maximum mass, minimum distance)  $\rightarrow (M = 4.059 \times 10^6 M_\odot, D = 7.868$  kpc [Fig. 7(c)]).

The dilaton parameter required to reproduce the central value of the EHT estimated critical curve angular diameter of  $48.7 \mu\text{as}$  (denoted by the red solid line in Fig. 7) is  $0 \lesssim r_2 \lesssim 0.1$  for the first case [Fig. 7(a)],  $0.1 \lesssim r_2 \lesssim 0.2$  for the second case [Fig. 7(b)], and  $0.3 \lesssim r_2 \lesssim 0.4$  for the third case [Fig. 7(c)]. The allowed

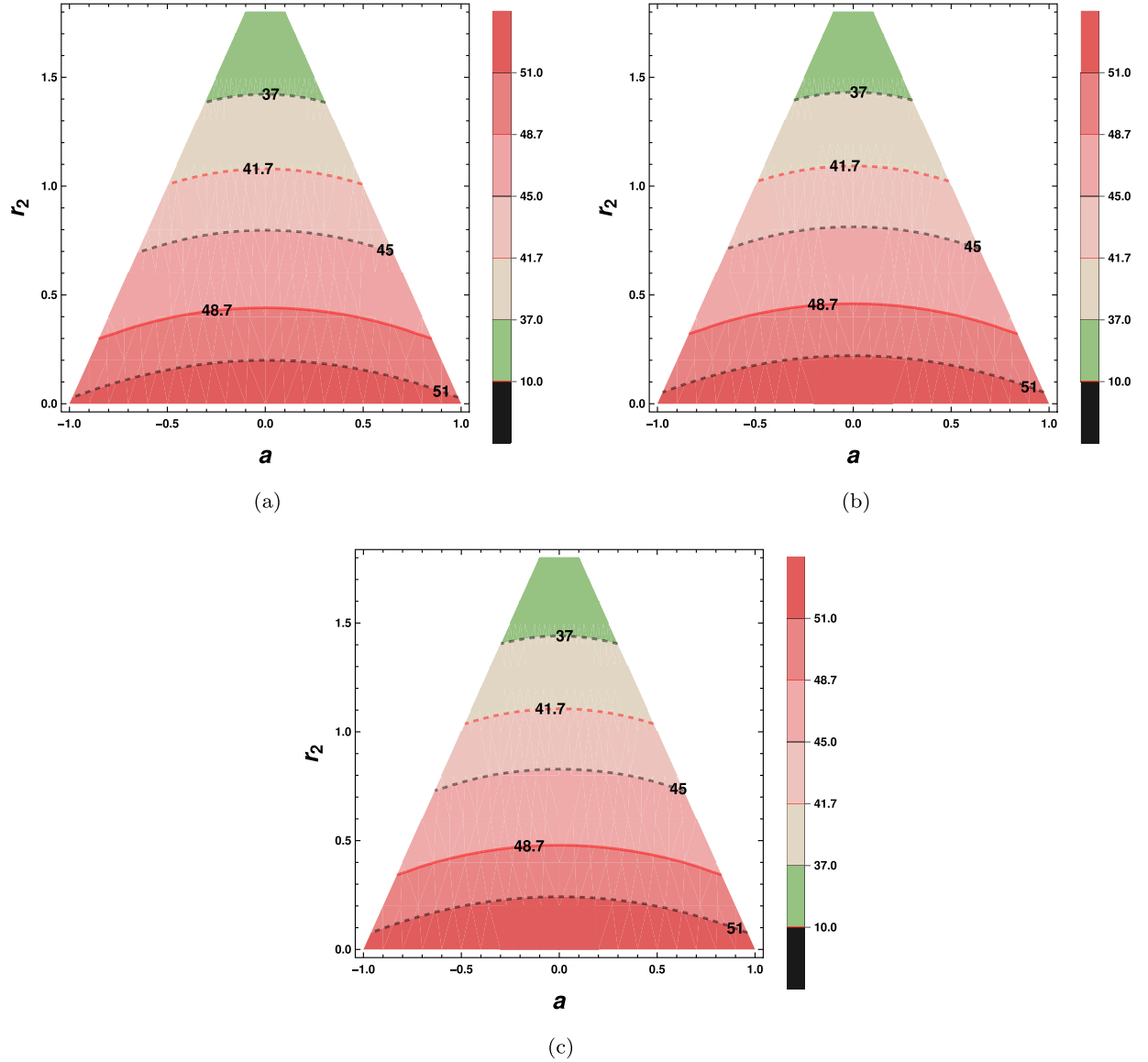


FIG. 9. (a) The above figure demonstrates the variation of the critical curve angular diameter of Sgr A\* with  $r_2$  and  $a$  assuming  $M = 4.249 \times 10^6 M_\odot$  and  $D = 8.256$  kpc. (b) The above figure demonstrates the variation of the critical curve angular diameter of Sgr A\* with  $r_2$  and  $a$  assuming  $M = 4.261 \times 10^6 M_\odot$  and  $D = 8.2467$  kpc. (c) The above figure demonstrates the variation of critical curve angular diameter of Sgr A\* with  $r_2$  and  $a$  assuming  $M = 4.273 \times 10^6 M_\odot$  and  $D = 8.2374$  kpc. Contour plots for angular diameter of critical curve of Sgr A\* for  $M = (4.261 \pm 0.012) \times 10^6 M_\odot$  and  $D = (8246.7 \pm 9.3)$  pc. In order to compute the angular diameter the inclination angle is taken to be  $\theta_0 = 46^\circ$ . The EHT inferred critical curve angular diameter ( $\Delta\theta = 48.7 \pm 7 \mu\text{as}$ ) is represented by the red contour lines (the red solid line corresponds to the central value while the  $1\text{-}\sigma$  contours are represented by the red dashed lines).

range of  $r_2$  is thus  $0 \lesssim r_2 \lesssim 0.4$  when the central value of the critical curve angular diameter is considered (i.e.,  $\Delta\theta = 48.7 \mu\text{as}$ ). When the  $1\text{-}\sigma$  interval in the angular diameter of the critical curve is taken into account (i.e.,  $48.7 \pm 7 \mu\text{as}$ , denoted by the red dashed lines in Fig. 7), the allowed range of  $r_2$  turns out to be (a)  $0 \lesssim r_2 \lesssim 0.8$  [Case 1, Fig. 7(a)], (b)  $0 \lesssim r_2 \lesssim 1$  [Case 2, Fig. 7(b)], and (c)  $0 \lesssim r_2 \lesssim 1.1$  [Case 3, Fig. 7(c)].

(2) When the redshift parameter is fixed to unity the distance and mass estimates by the Keck team yield  $D = (7935 \pm 50)$  pc and  $M = (3.951 \pm 0.047) \times 10^6 M_\odot$  [117] respectively. In order to calculate the theoretical angular diameter once again we consider

- (i) (minimum mass, maximum distance)  $\rightarrow (M = 3.904 \times 10^6 M_\odot, D = 7.985$  kpc [Fig. 8(a)]).
- (ii) (central mass, central distance)  $\rightarrow (M = 3.951 \times 10^6 M_\odot, D = 7.935$  kpc [Fig. 8(b)]).
- (iii) (maximum mass, minimum distance)  $\rightarrow (M = 3.998 \times 10^6 M_\odot, D = 7.885$  kpc [Fig. 8(c)]).



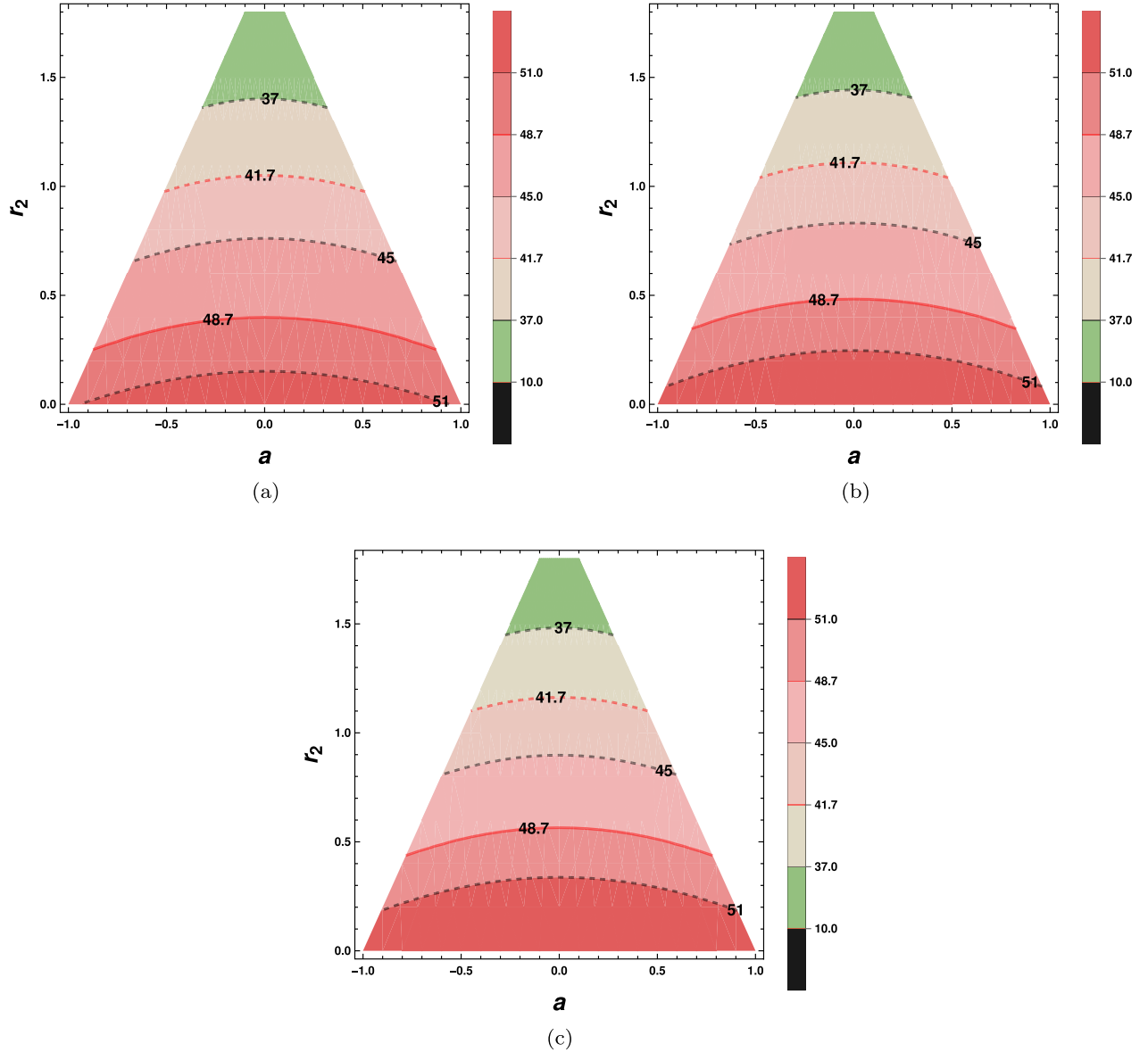


FIG. 10. (a) The above figure demonstrates the variation of the critical curve angular diameter of Sgr A\* with  $r_2$  and  $a$  assuming  $M = 4.245 \times 10^6 M_\odot$  and  $D = 8.319$  kpc. (b) The above figure demonstrates the variation of the critical curve angular diameter of Sgr A\* with  $r_2$  and  $a$  assuming  $M = 4.297 \times 10^6 M_\odot$  and  $D = 8.277$  kpc. (c) The above figure demonstrates the variation of the critical curve angular diameter of Sgr A\* with  $r_2$  and  $a$  assuming  $M = 4.349 \times 10^6 M_\odot$  and  $D = 8.235$  kpc. Contour plots for the angular diameter of the critical curve of Sgr A\* for  $M = (4.297 \pm 0.012 \pm 0.04) \times 10^6 M_\odot$  and  $D = (8277 \pm 9 \pm 33)$  pc. In order to compute the angular diameter the inclination angle is taken to be  $\theta_0 = 46^\circ$ . The EHT inferred critical curve angular diameter ( $\Delta\theta = 48.7 \pm 7 \mu\text{as}$ ) is represented by the red contour lines (the red solid line corresponds to the central value while the  $1\text{-}\sigma$  contours are represented by the red dashed lines).

We first discuss constraints on  $r_2$  based on the central value, i.e.,  $\Delta\theta = 48.7 \mu\text{as}$  (denoted by the red solid line in Fig. 8). With minimum mass ( $M = 3.904 \times 10^6 M_\odot$ ) and maximum distance ( $D = 7.985$  kpc), the allowed range of  $r_2$  turns out to be  $0 \lesssim r_2 \lesssim 0.1$  [Fig. 8(a)]. When the central value of mass ( $M = 3.951 \times 10^6 M_\odot$ ) and distance ( $D = 7.935$  kpc) are considered the allowed range of  $r_2$  turns out to be  $0.1 \lesssim r_2 \lesssim 0.2$  [Fig. 8(b)]. Finally, with maximum mass ( $M = 3.998 \times 10^6$ ) and minimum distance

( $D = 7.885$  kpc) the allowed range of  $r_2$  turns out to be  $0.2 \lesssim r_2 \lesssim 0.3$  [Fig. 8(c)]. In this case the observationally preferred range of  $r_2$  is thus  $0 \lesssim r_2 \lesssim 0.3$  when the central value of the observed angular diameter is considered. When the  $1\text{-}\sigma$  interval in the critical curve angular diameter is taken into account (i.e.,  $48.7 \pm 7 \mu\text{as}$ , denoted by the red dashed lines in Fig. 8), the allowed range of  $r_2$  turns out to be (a)  $0 \lesssim r_2 \lesssim 0.9$  [Case 1, Fig. 8(a), and Case 2, Fig. 8(b)] and (b)  $0 \lesssim r_2 \lesssim 1$  [Case 3, Fig. 8(c)].

The above discussion elucidates that in both the mass and distance measurements by the Keck team (i.e., redshift parameter free or fixed to unity), when the central values of the two aforesaid quantities are considered, a nonvanishing dilaton charge ( $0.1 \lesssim r_2 \lesssim 0.2$ ) is required when one attempts to explain the central value of the EHT estimated critical curve angular diameter i.e.,  $48.7 \mu\text{s}$ . However, when one takes into account the errors in mass and distance along with the  $1-\sigma$  interval in the critical curve angular diameter, the Kerr scenario is included.

We next discuss constrains on  $r_2$  assuming distance and mass estimates by the GRAVITY Collaboration [118,119]:

- (1) According to the results of the GRAVITY Collaboration the mass and distance of Sgr A\* turn out to be  $M = (4.261 \pm 0.012) \times 10^6 M_\odot$  and  $D = (8246.7 \pm 9.3) \text{ pc}$  [118,119] respectively. As done earlier, we use this mass and distance along with their  $1-\sigma$  intervals to establish constrains on the preferred range of  $r_2$ . Once again, we report constrains on  $r_2$  based on the EHT inferred critical curve angular diameter  $\Delta\theta = 48.7 \pm 7 \mu\text{s}$ . The central value of this observed angular diameter, i.e.,  $\Delta\theta = 48.7 \mu\text{s}$  (denoted by the red solid line in Fig. 9) can be explained by  $0.3 \lesssim r_2 \lesssim 0.4$  irrespective of whether
  - (i) The minimum mass ( $M = 4.249 \times 10^6 M_\odot$ ) and maximum distance ( $D = 8.256 \text{ kpc}$ ) are considered [Fig. 9(a)],
  - (ii) The central value of mass ( $M = 4.261 \times 10^6 M_\odot$ ) and distance ( $D = 8.2467 \text{ kpc}$ ) is considered [Fig. 9(b)] or
  - (iii) The maximum mass ( $M = 4.273 \times 10^6 M_\odot$ ) and minimum distance ( $D = 8.2374 \text{ kpc}$ ) are considered [Fig. 9(c)].

Since in this case, the  $1-\sigma$  intervals associated with mass and distance are small compared to the central value, the constrain on  $r_2$  ( $0.3 \lesssim r_2 \lesssim 0.4$ ) does not vary appreciably with mass and distance. When one considers the  $1-\sigma$  interval in the critical curve angular diameter (i.e.,  $48.7 \pm 7 \mu\text{s}$ , denoted by the red dashed lines in Fig. 9), the allowed range of  $r_2$  turns out to be (a)  $0 \lesssim r_2 \lesssim 1$  for Case 1 [Fig. 9(a)] and Case 2 [Fig. 9(b)] and (b)  $0 \lesssim r_2 \lesssim 1.1$  for Case 3, [Fig. 9(c)].

(2) When one takes into account the systematics due to optical aberrations, the GRAVITY Collaboration constrains the mass and distance of Sgr A\* to  $M = (4.297 \pm 0.012 \pm 0.040) \times 10^6 M_\odot$  and  $D = (8277 \pm 9 \pm 33) \text{ pc}$  respectively. Once again, the theoretical angular diameter of the critical curve is calculated with

- (i) The minimum mass ( $M = 4.245 \times 10^6 M_\odot$ ) and maximum distance ( $D = 8.319 \text{ kpc}$ ) [Fig. 10(a)],
- (ii) The central value of mass ( $M = 4.297 \times 10^6 M_\odot$ ) and distance ( $D = 8.277 \text{ kpc}$ ) [Fig. 10(b)], and with
- (iii) The maximum mass ( $M = 4.349 \times 10^6 M_\odot$ ) and minimum distance ( $D = 8.235 \text{ kpc}$ ) [Fig. 10(c)].

We note that, in order to explain the central value of the EHT inferred critical curve angular diameter ( $\Delta\theta = 48.7 \mu\text{s}$ , i.e., red solid line in Fig. 10), the required dilaton parameter corresponds to (a)  $0.25 \lesssim r_2 \lesssim 0.3$  for Case 1 [Fig. 10(a)], (b)  $0.3 \lesssim r_2 \lesssim 0.4$  for Case 2 [Fig. 10(b)], and (c)  $0.4 \lesssim r_2 \lesssim 0.5$  for Case 3 [Fig. 10(c)]. The observationally allowed range of  $r_2$  thus corresponds to  $0.25 \lesssim r_2 \lesssim 0.5$  when the central value of the critical curve angular diameter is considered. When one takes into account the  $1-\sigma$

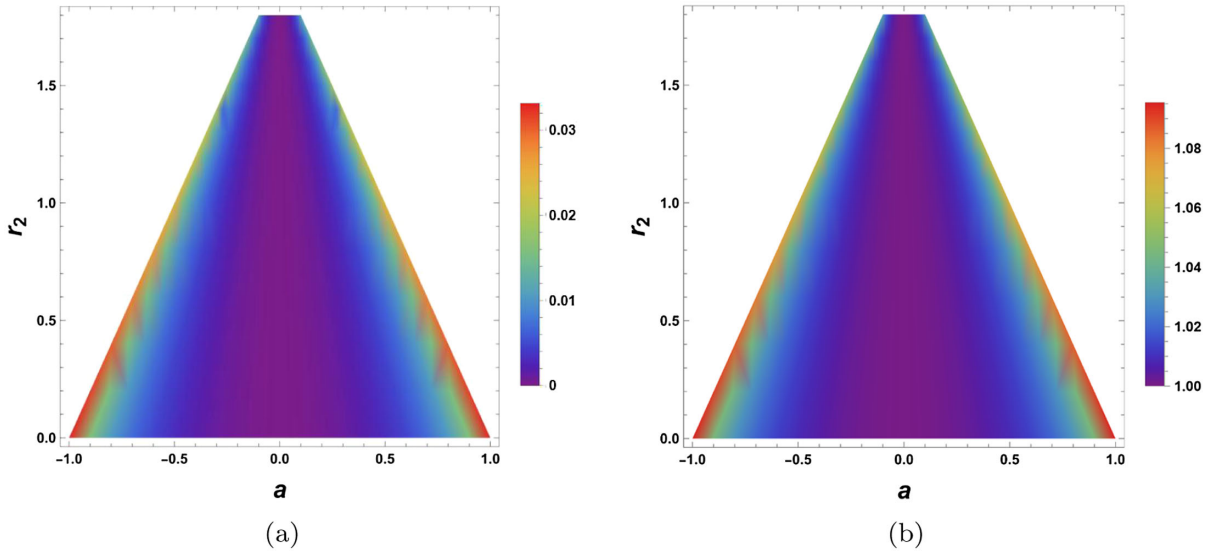


FIG. 11. (a) Figure illustrating dependence of  $\Delta C$  on  $r_2$  and  $a$  assuming an inclination angle of  $46^\circ$  corresponding to Sgr A\*. (b) Figure illustrating dependence of  $\Delta A$  on  $r_2$  and  $a$  assuming an inclination angle of  $46^\circ$  corresponding to Sgr A\*. The above figure depicts the variation of  $\Delta C$  and  $\Delta A$  as function of  $r_2$  and  $a$ , for the source Sgr A\*.

interval in the EHT estimated critical curve angular diameter (i.e.,  $48.7 \pm 7 \mu\text{as}$ ) the allowed range of  $r_2$  turns out to be (a)  $0 \lesssim r_2 \lesssim 1$  for Case 1 [Fig. 10(a)], (b)  $0 \lesssim r_2 \lesssim 1.1$  for Case 2 [Fig. 10(b)], and (c)  $0 \lesssim r_2 \lesssim 1.2$  for Case 3 [Fig. 10(c)].

From the above discussion we note that, considering both the mass and distance measurements by the GRAVITY Collaboration (with and without optical aberration), the central value of the EHT estimated critical curve angular diameter ( $48.7 \mu\text{as}$ ) can be explained by only nonzero values of the dilaton parameter ( $0.25 \lesssim r_2 \lesssim 0.5$ ). This result holds even when the errors in the mass and distance are taken into account. The Kerr scenario is however allowed when the  $1\text{-}\sigma$  error bars in the critical curve angular diameter (i.e.,  $48.7 \pm 7 \mu\text{as}$ ) are considered.

Thus, taking into account the mass and distance estimates by both the Keck team and the GRAVITY Collaboration, one may conclude that the image of Sgr A\* shows a preference toward the Kerr-Sen scenario although the general relativistic case is allowed when the errors in mass and distance are taken into account or the  $1\text{-}\sigma$  interval in the derived critical curve angular diameter is considered.

For completeness we plot in Fig. 11 the dependence of the deviation from circularity  $\Delta C$  and the axis ratio  $\Delta A$  on the metric parameters  $r_2$  and  $a$ . This is a theoretical plot which only requires an independent estimate of the inclination of the source, which is taken to be  $\theta_0 = 46^\circ$  as discussed earlier. The EHT team has not provided any data related to  $\Delta A$  and  $\Delta C$  for Sgr A\*. These results therefore cannot impose additional constraints on the dilaton parameter  $r_2$  at present. These plots can however be useful in the future when the EHT releases data pertaining to  $\Delta A$  and  $\Delta C$  for Sgr A\*.

## V. CONCLUDING REMARKS

In this work we investigate the signatures of EMDA gravity from the observed images of M87\* and Sgr A\*. EMDA gravity arises in the low-energy effective action of superstring theories, and exploring its astrophysical implications is important as this can potentially provide a possibility to test string inspired models. The Kerr-Sen spacetime corresponds to the stationary, charged, and axisymmetric black hole solution of EMDA gravity [73]. In our work, we constrain the dilaton parameter  $r_2$  (related to the charge of the Kerr-Sen black hole) by using the angular diameter of the critical curve (which is derived from the observed ring) of M87\* [7] and Sgr A\* [13], reported by the EHT Collaboration. In the event of a vanishing dilaton charge, the Kerr scenario is recovered.

The theoretically calculated angular diameter of the critical curve depends on the mass  $M$ , distance  $D$ , inclination angle  $\theta_0$ , and the nature of the background spacetime. In this work we assumed the background spacetime to be described by the Kerr-Sen metric. We used previously measured values of  $M$ ,  $D$ , and  $\theta_0$  for M87\* and Sgr A\* in

our work. The errors in mass and distance are taken into account while deriving constraints on the dilaton parameter  $r_2$ . We however keep the inclination angle fixed to the central value as the errors in the inclination angle turn out to be small.

We first discuss the allowed range of  $r_2$  from the observed image of M87\*. The observed ring diameter is  $42 \pm 3 \mu\text{as}$ , while the EHT inferred critical curve angular diameter can be as small as  $(37.8 \pm 3) \mu\text{as}$ . We use previously determined  $M$ ,  $D$ , and  $\theta_0$  for M87\* to theoretically estimate the critical curve angular diameter. The inclination angle of M87\* is  $\theta_0 = (17 \pm 2)^\circ$  while its distance is  $16.8 \pm 0.8 \text{ Mpc}$ . We use the central value, i.e.,  $\theta_0 = 17^\circ$  (see discussion above) and take into account the  $1\text{-}\sigma$  interval in  $D$  in our analysis. The mass of M87\* has been independently estimated based on stellar dynamics and gas dynamics studies. We note that, with mass of M87\* estimated from gas dynamics studies ( $M = 3.5_{-0.3}^{+0.9} \times 10^9 M_\odot$ ) [8,116] the inferred critical curve angular diameter of  $(37.8 \pm 3) \mu\text{as}$  cannot be reproduced even when the theoretical critical curve is calculated with maximum mass ( $M = 4.4 \times 10^9 M_\odot$ ) and minimum distance (16 Mpc). Therefore, this mass measurement probably needs to be revisited.

When the mass of M87\* based on stellar dynamics measurements ( $M = 6.2_{-0.6}^{+1.1} \times 10^9 M_\odot$ ) is used to compute the theoretical critical curve angular diameter, (i)  $0.8 \lesssim r_2 \lesssim 1$  is required to explain the inferred  $\Delta\theta = 37.8 \mu\text{as}$  when maximum mass ( $M = 7.3 \times 10^9 M_\odot$ ) and minimum distance (16 Mpc) are considered, (ii)  $r_2 \simeq 0$  is required, when the central value of mass ( $M = 6.2 \times 10^9 M_\odot$ ) and distance (16.8 Mpc) are considered, (iii) while no suitable value of  $r_2$  can explain the inferred  $\Delta\theta = 37.8 \mu\text{as}$  (even within  $1\text{-}\sigma$ , i.e.,  $\Delta\theta = 37.8 \pm 3 \mu\text{as}$ ) when minimum mass ( $M = 5.6 \times 10^9 M_\odot$ ) and maximum distance (17.6 Mpc) are considered. Thus, in this case, the Kerr scenario is preferred although nonzero dilaton charge is also allowed when errors in mass and distance are taken into account or the  $1\text{-}\sigma$  interval in the derived critical curve angular diameter is considered (see Sec. IV). Here, it may be worthwhile to mention that the Kerr solution is not unique to GR but arises even in several other alternative gravity scenarios [80,81].

The EHT Collaboration has also released the image of Sgr A\* and reported that the angular diameter of the critical curve derived from the observed ring is  $(48.7 \pm 7) \mu\text{as}$ . The inclination angle of Sgr A\* from previous measurements is  $\theta_0 = 46^\circ$  [120]. The mass and distance of this source are well constrained by the Keck team and the GRAVITY Collaboration.

We first report observational constraints on  $r_2$  assuming distance and mass estimated by the Keck team. Keeping the redshift parameter free, the Keck team reports the mass and distance of Sgr A\* to be  $M = (3.975 \pm 0.058 \pm 0.026) \times 10^6 M_\odot$  and  $D = (7959 \pm 59 \pm 32) \text{ pc}$ , respectively. The dilaton parameter required to reproduce the central

value of the inferred critical curve angular diameter ( $\Delta\theta = 48.7 \mu\text{as}$ ) is  $0.1 \lesssim r_2 \lesssim 0.2$  for the central value of mass ( $M = 3.975 \times 10^6 M_\odot$ ) and distance ( $D = 7959 \text{ pc}$ ) [Fig. 7(b)]. When errors in the mass and distance are considered the allowed range of  $r_2$  turns out to be  $0 \lesssim r_2 \lesssim 0.4$ . When one further considers the  $1\text{-}\sigma$  interval in the inferred critical curve angular diameter ( $48.7 \pm 7 \mu\text{as}$ ) along with the errors in the estimated mass and distance, then the maximum allowed range of  $r_2$  turns out to be  $0 \lesssim r_2 \lesssim 1.1$ .

When the redshift parameter is fixed to unity, the distance and mass estimates by the Keck team are  $D = (7935 \pm 50) \text{ pc}$  and  $M = (3.951 \pm 0.047) \times 10^6 M_\odot$  respectively. As before, we first discuss constraints on  $r_2$  assuming  $\Delta\theta = 48.7 \mu\text{as}$ . When the central value of mass ( $M = 3.951 \times 10^6 M_\odot$ ) and distance ( $D = 7.935 \text{ kpc}$ ) are considered, the allowed range of  $r_2$  turns out to be  $0.1 \lesssim r_2 \lesssim 0.2$  [Fig. 8(b)]. With errors in mass and distance taken into account, the allowed range of  $r_2$  becomes  $0 \lesssim r_2 \lesssim 0.3$ . When the  $1\text{-}\sigma$  intervals in the mass, distance, and the inferred critical curve angular diameter ( $48.7 \pm 7 \mu\text{as}$ ) are taken into account, then the maximum allowed range of  $r_2$  turns out to be  $0 \lesssim r_2 \lesssim 1$ .

We next discuss constraints on  $r_2$  assuming distance and mass estimates by the GRAVITY Collaboration [118,119]. According to the results of the GRAVITY Collaboration, the mass and distance of Sgr A\* turn out to be  $M = (4.261 \pm 0.012) \times 10^6 M_\odot$  and  $D = (8246.7 \pm 9.3) \text{ pc}$  [118,119] respectively. Once again, we first report constraints on  $r_2$  based on the central value of the derived critical curve angular diameter ( $48.7 \mu\text{as}$ ). Our analysis reveals that  $\Delta\theta = 48.7 \mu\text{as}$  can be explained by  $0.3 \lesssim r_2 \lesssim 0.4$  even when  $1\text{-}\sigma$  intervals in mass and distance are considered. Considering the  $1\text{-}\sigma$  interval in the angular diameter ( $\Delta\theta = 48.7 \pm 7 \mu\text{as}$ ) along with the errors in mass and distance, the maximum allowed range of  $r_2$  turns out to be  $0 \lesssim r_2 \lesssim 1.1$ .

When one takes into account the systematics due to optical aberrations, the GRAVITY Collaboration constrains the mass and distance of Sgr A\* to  $M = (4.297 \pm 0.012 \pm 0.040) \times 10^6 M_\odot$  and  $D = (8277 \pm 9 \pm 33) \text{ pc}$  respectively. In order to explain  $\Delta\theta = 48.7 \mu\text{as}$ , the required dilaton parameter corresponds to  $0.3 \lesssim r_2 \lesssim 0.4$  when the central value of mass ( $M = 4.297 \times 10^6 M_\odot$ ) and distance ( $D = 8.277 \text{ kpc}$ ) are considered. Taking into account the errors in mass and distance,  $0.25 \lesssim r_2 \lesssim 0.5$  is required to reproduce  $\Delta\theta = 48.7 \mu\text{as}$ . When one considers the  $1\text{-}\sigma$  interval in the angular diameter ( $\Delta\theta = 48.7 \pm 7 \mu\text{as}$ ) in addition to the errors in mass and distance, the maximum allowed range of  $r_2$  turns out to be  $0 \lesssim r_2 \lesssim 1.2$ .

Therefore, when the theoretical critical curve angular diameter is calculated with the central value of all four of the mass and distance estimates of Sgr A\*, a positive dilaton parameter better explains the central value of the derived critical curve angular diameter ( $\Delta\theta = 48.7 \mu\text{as}$ ). This implies that the observed image of Sgr A\* shows a preference toward the Kerr-Sen scenario although the Kerr scenario is included when the errors in mass and distance are taken into account or the  $1\text{-}\sigma$  interval in the derived critical curve angular diameter is considered.

It may be worthwhile to mention some limitations of our methodology. First, the critical curve is not directly observable; it is derived from the observed ring using various model dependent simulations. Thus, the constraints on  $r_2$  can be further improved, when simulations with improved models are used to estimate quantities related to the critical curve. Secondly, we have considered error bars in mass, distance, and angular diameter of the critical curve in finding constraints on  $r_2$ . With more precise measurements (i.e., lower error bars) the constraints on  $r_2$  can be further improved.

The charge of the Kerr-Sen black hole has been constrained previously from different astrophysical observations, e.g., the black hole continuum spectrum [122] and relativistic jets [123]. A comparison of the theoretical spectrum of eighty Palomar Green quasars with their optical observations reveals that  $r_2 \sim 0.2$  best explains the observations. The general relativistic scenario with  $r_2 = 0$  is however included when the  $1\text{-}\sigma$  interval is considered [122]. When the jet power associated with ballistic jets in microquasars is used to constrain the dilaton parameter,  $r_2 \simeq 0$  seem to be favored by observations [123]. The reflection spectrum of black holes has given an upper bound  $r_2 < 0.011$  with 90% confidence limit which weakly favors the Kerr-Sen scenario [91]. Thus, we note that astrophysical observations, e.g., black hole images, continuum spectra, or jets either indicate a small/moderate dilatonic charge in black holes or exhibit a preference toward the Kerr scenario. The scope to verify this finding will further increase as EHT releases more black hole images with greater resolution.

## ACKNOWLEDGMENTS

Research of I. B. is funded by the Start-Up Research Grant from SERB, DST, Government of India (Reg. No. SRG/2021/000418). The authors sincerely thank the anonymous referee for suggestions and feedback which has considerably improved the paper.

- [1] Steven Weinberg, *Gravitation and Cosmology: Principles and Applications of the General Theory of Relativity* (John Wiley and Sons, New York, 1972), ISBN 978-0-471-92567-5, 978-0-471-92567-5.
- [2] Clifford M. Will, The confrontation between general relativity and experiment, *Living Rev. Relativity* **17**, 4 (2014).
- [3] C. M. Will, *Theory and Experiment in Gravitational Physics* (Cambridge University Press, Cambridge, 1993), ISBN 9780521439732.
- [4] B. P. Abbott *et al.*, Observation of gravitational waves from a binary black hole merger, *Phys. Rev. Lett.* **116**, 061102 (2016).
- [5] B. P. Abbott *et al.*, GW170817: Observation of gravitational waves from a binary neutron star inspiral, *Phys. Rev. Lett.* **119**, 161101 (2017).
- [6] B. P. Abbott *et al.*, GWTC-1: A gravitational-wave transient catalog of compact binary mergers observed by LIGO and Virgo during the first and second observing runs, *Phys. Rev. X* **9**, 031040 (2019).
- [7] Kazunori Akiyama *et al.*, First M87 event horizon telescope results. I. The shadow of the supermassive black hole, *Astrophys. J. Lett.* **875**, L1 (2019).
- [8] Kazunori Akiyama *et al.*, First M87 event horizon telescope results. VI. The shadow and mass of the central black hole, *Astrophys. J. Lett.* **875**, L6 (2019).
- [9] Kazunori Akiyama *et al.*, First M87 event horizon telescope results. V. Physical origin of the asymmetric ring, *Astrophys. J. Lett.* **875**, L5 (2019).
- [10] Kazunori Akiyama *et al.*, First M87 event horizon telescope results. II. Array and instrumentation, *Astrophys. J. Lett.* **875**, L2 (2019).
- [11] Kazunori Akiyama *et al.*, First M87 event horizon telescope results. III. Data processing and calibration, *Astrophys. J. Lett.* **875**, L3 (2019).
- [12] Kazunori Akiyama *et al.*, First M87 event horizon telescope results. IV. Imaging the central supermassive black hole, *Astrophys. J. Lett.* **875**, L4 (2019).
- [13] Kazunori Akiyama *et al.*, First Sagittarius A\* event horizon telescope results. I. The shadow of the supermassive black hole in the center of the Milky Way, *Astrophys. J. Lett.* **930**, L12 (2022).
- [14] Kazunori Akiyama *et al.*, First Sagittarius A\* event horizon telescope results. II. EHT and multiwavelength observations, data processing, and calibration, *Astrophys. J. Lett.* **930**, L13 (2022).
- [15] Kazunori Akiyama *et al.*, First Sagittarius A\* event horizon telescope results. III. Imaging of the Galactic center supermassive black hole, *Astrophys. J. Lett.* **930**, L14 (2022).
- [16] Kazunori Akiyama *et al.*, First Sagittarius A\* event horizon telescope results. IV. Variability, morphology, and black hole mass, *Astrophys. J. Lett.* **930**, L15 (2022).
- [17] Kazunori Akiyama *et al.*, First Sagittarius A\* event horizon telescope results. V. Testing astrophysical models of the Galactic center black hole, *Astrophys. J. Lett.* **930**, L16 (2022).
- [18] Kazunori Akiyama *et al.*, First Sagittarius A\* event horizon telescope results. VI. Testing the black hole metric, *Astrophys. J. Lett.* **930**, L17 (2022).
- [19] Roger Penrose, Gravitational collapse and space-time singularities, *Phys. Rev. Lett.* **14**, 57 (1965).
- [20] S. W. Hawking, Breakdown of predictability in gravitational collapse, *Phys. Rev. D* **14**, 2460 (1976).
- [21] S. W. Hawking and G. F. R. Ellis, *The Large Scale Structure of Space-Time*, Cambridge Monographs on Mathematical Physics (Cambridge University Press, Cambridge, England, 2011), ISBN 978-0-521-20016-5, 978-0-521-09906-6, 978-0-511-82630-6, 978-0-521-09906-6, [10.1017/CBO9780511524646](https://doi.org/10.1017/CBO9780511524646).
- [22] Robert M. Wald, *General Relativity* (Chicago University Press, Chicago, USA, 1984), [10.7208/chicago/9780226870373.001.0001](https://doi.org/10.7208/chicago/9780226870373.001.0001).
- [23] Demetrios Christodoulou, The formation of black holes and singularities in spherically symmetric gravitational collapse, *Commun. Pure Appl. Math.* **44**, 339 (1991).
- [24] Carlo Rovelli, Black hole entropy from loop quantum gravity, *Phys. Rev. Lett.* **77**, 3288 (1996).
- [25] Fay Dowker, Causal sets and the deep structure of spacetime, in *100 Years Of Relativity: Space-Time Structure: Einstein and Beyond*, edited by Abhay Ashtekar (World Scientific Publishing, 2005), pp. 445–464, [10.1142/9789812700988\\_0016](https://doi.org/10.1142/9789812700988_0016).
- [26] Abhay Ashtekar, Tomasz Pawłowski, and Parampreet Singh, Quantum nature of the big bang, *Phys. Rev. Lett.* **96**, 141301 (2006).
- [27] Dawood Kothawala, Minimal length and small scale structure of spacetime, *Phys. Rev. D* **88**, 104029 (2013).
- [28] E. P. Wigner, *The Basic Conflict Between the Concepts of General Relativity and of Quantum Mechanics* (Springer Berlin Heidelberg, Berlin, Heidelberg, 1997), pp. 350–350, ISBN 978-3-662-09203-3, [10.1007/978-3-662-09203-3\\_33](https://doi.org/10.1007/978-3-662-09203-3_33).
- [29] M. Milgrom, A modification of the Newtonian dynamics: Implications for galaxies, *Astrophys. J.* **270**, 371 (1983).
- [30] J. Bekenstein and Mordehai Milgrom, Does the missing mass problem signal the breakdown of Newtonian gravity?, *Astrophys. J.* **286**, 7 (1984).
- [31] Mordehai Milgrom and Robert H. Sanders, MOND and the dearth of dark matter in ordinary elliptical galaxies, *Astrophys. J.* **599**, L25 (2003).
- [32] Timothy Clifton, Pedro G. Ferreira, Antonio Padilla, and Constantinos Skordis, Modified gravity and cosmology, *Phys. Rep.* **513**, 1 (2012).
- [33] S. Perlmutter *et al.*, Measurements of  $\Omega$  and  $\Lambda$  from 42 high redshift supernovae, *Astrophys. J.* **517**, 565 (1999).
- [34] Adam G. Riess *et al.*, Observational evidence from supernovae for an accelerating Universe and a cosmological constant, *Astron. J.* **116**, 1009 (1998).
- [35] S. D. Odintsov and V. K. Oikonomou, Unification of inflation with dark energy in  $f(R)$  gravity and axion dark matter, *Phys. Rev. D* **99**, 104070 (2019).
- [36] Shin'ichi Nojiri, S. D. Odintsov, and V. K. Oikonomou,  $F(R)$  gravity with an axion-like particle: Dynamics, gravity waves, late and early-time phenomenology, *Ann. Phys. (Amsterdam)* **418**, 168186 (2020).
- [37] S. D. Odintsov and V. K. Oikonomou, Geometric inflation and dark energy with axion  $F(R)$  gravity, *Phys. Rev. D* **101**, 044009 (2020).

- [38] S. D. Odintsov and V. K. Oikonomou, Aspects of axion  $F(R)$  gravity, *Europhys. Lett.* **129**, 40001 (2020).
- [39] Thomas P. Sotiriou and Valerio Faraoni,  $f(R)$  theories of gravity, *Rev. Mod. Phys.* **82**, 451 (2010).
- [40] Antonio De Felice and Shinji Tsujikawa,  $f(R)$  theories, *Living Rev. Relativity* **13**, 3 (2010).
- [41] Salvatore Capozziello and Mariafelicia De Laurentis, Extended theories of gravity, *Phys. Rep.* **509**, 167 (2011).
- [42] Roy Maartens, Brane world gravity, *Living Rev. Relativity* **7**, 7 (2004).
- [43] J. M. Overduin and P. S. Wesson, Kaluza-Klein gravity, *Phys. Rep.* **283**, 303 (1997).
- [44] Tsutomu Kobayashi, Horndeski theory and beyond: A review, *Rep. Prog. Phys.* **82**, 086901 (2019).
- [45] R. T. Hammond, Torsion gravity, *Rep. Prog. Phys.* **65**, 599 (2002).
- [46] Shin'ichi Nojiri and Sergei D. Odintsov, Unified cosmic history in modified gravity: From  $F(R)$  theory to Lorentz non-invariant models, *Phys. Rep.* **505**, 59 (2011).
- [47] S. Nojiri, S. D. Odintsov, and V. K. Oikonomou, Modified gravity theories on a nutshell: Inflation, bounce and late-time evolution, *Phys. Rep.* **692**, 1 (2017).
- [48] Emanuele Berti *et al.*, Testing general relativity with present and future astrophysical observations, *Classical Quantum Gravity* **32**, 243001 (2015).
- [49] Dimitrios Psaltis, Probes and tests of strong-field gravity with observations in the electromagnetic spectrum, *Living Rev. Relativity* **11**, 9 (2008).
- [50] Shin'ichi Nojiri and Sergei D. Odintsov, Modified gravity with negative and positive powers of the curvature: Unification of the inflation and of the cosmic acceleration, *Phys. Rev. D* **68**, 123512 (2003).
- [51] Shin'ichi Nojiri and Sergei D. Odintsov, Modified  $f(R)$  gravity consistent with realistic cosmology: From matter dominated epoch to dark energy Universe, *Phys. Rev. D* **74**, 086005 (2006).
- [52] Salvatore Capozziello, S. Nojiri, S. D. Odintsov, and A. Troisi, Cosmological viability of  $f(R)$ -gravity as an ideal fluid and its compatibility with a matter dominated phase, *Phys. Lett. B* **639**, 135 (2006).
- [53] Cornelius Lanczos, Electricity as a natural property of Riemannian geometry, *Rev. Mod. Phys.* **39**, 716 (1932).
- [54] Cornelius Lanczos, A remarkable property of the Riemann-Christoffel tensor in four dimensions, *Ann. Math.* **39**, 842 (1938).
- [55] David Lovelock, The Einstein tensor and its generalizations, *J. Math. Phys. (N.Y.)* **12**, 498 (1971).
- [56] T. Padmanabhan and D. Kothawala, Lanczos-Lovelock models of gravity, *Phys. Rep.* **531**, 115 (2013).
- [57] Tetsuya Shiromizu, Kei-ichi Maeda, and Misao Sasaki, The Einstein equation on the 3-brane world, *Phys. Rev. D* **62**, 024012 (2000).
- [58] Naresh Dadhich, Roy Maartens, Philippos Papadopoulos, and Vahid Rezanian, Black holes on the brane, *Phys. Lett. B* **487**, 1 (2000).
- [59] T. Harko and M. K. Mak, Vacuum solutions of the gravitational field equations in the brane world model, *Phys. Rev. D* **69**, 064020 (2004).
- [60] T. R. P. Carames, M. E. X. Guimaraes, and J. M. Hoff da Silva, Effective gravitational equations for  $f(R)$  brane-world models, *Phys. Rev. D* **87**, 106011 (2013).
- [61] Tsutomu Kobayashi, Tetsuya Shiromizu, and Nathalie Deruelle, Low energy effective gravitational equations on a Gauss-Bonnet brane, *Phys. Rev. D* **74**, 104031 (2006).
- [62] Sumanta Chakraborty and Soumitra SenGupta, Spherically symmetric brane spacetime with bulk  $f(\mathcal{R})$  gravity, *Eur. Phys. J. C* **75**, 11 (2015).
- [63] Sumanta Chakraborty and Soumitra SenGupta, Effective gravitational field equations on  $m$ -brane embedded in  $n$ -dimensional bulk of Einstein and  $f(\mathcal{R})$  gravity, *Eur. Phys. J. C* **75**, 538 (2015).
- [64] Gregory Walter Horndeski, Second-order scalar-tensor field equations in a four-dimensional space, *Int. J. Theor. Phys.* **10**, 363 (1974).
- [65] Thomas P. Sotiriou and Shuang-Yong Zhou, Black hole hair in generalized scalar-tensor gravity, *Phys. Rev. Lett.* **112**, 251102 (2014).
- [66] Eugeny Babichev, Christos Charmousis, and Antoine Lehébel, Black holes and stars in Horndeski theory, *Classical Quantum Gravity* **33**, 154002 (2016).
- [67] Christos Charmousis and Minas Tsoukalas, Lovelock Galileons and black holes, *Phys. Rev. D* **92**, 104050 (2015).
- [68] Sourav Bhattacharya and Sumanta Chakraborty, Constraining some Horndeski gravity theories, *Phys. Rev. D* **95**, 044037 (2017).
- [69] Petr Horava and Edward Witten, Heterotic and type I string dynamics from eleven dimensions, *Nucl. Phys.* **B460**, 506 (1996).
- [70] Petr Horava and Edward Witten, Eleven-dimensional supergravity on a manifold with boundary, *Nucl. Phys.* **B475**, 94 (1996).
- [71] J. Polchinski, *String theory. Vol. 1: An Introduction to the Bosonic String*, Cambridge Monographs on Mathematical Physics (Cambridge University Press, Cambridge, England, 2007), ISBN 9780511252273, 9780521672276, 9780521633031, [10.1017/CBO9780511816079](https://doi.org/10.1017/CBO9780511816079).
- [72] J. Polchinski, *String Theory. Vol. 2: Superstring Theory and Beyond*, Cambridge Monographs on Mathematical Physics (Cambridge University Press, Cambridge, England, 2007), ISBN 9780511252280, 9780521633048, 9780521672283, [10.1017/CBO9780511618123](https://doi.org/10.1017/CBO9780511618123).
- [73] Ashoke Sen, Rotating charged black hole solution in heterotic string theory, *Phys. Rev. Lett.* **69**, 1006 (1992).
- [74] Julian Sonner and Paul K. Townsend, Recurrent acceleration in dilaton-axion cosmology, *Phys. Rev. D* **74**, 103508 (2006).
- [75] Riccardo Catena and Jan Moller, Axion-dilaton cosmology and dark energy, *J. Cosmol. Astropart. Phys.* **03** (2008) 012.
- [76] G. W. Gibbons and Kei-ichi Maeda, Black holes and membranes in higher dimensional theories with dilaton fields, *Nucl. Phys.* **B298**, 741 (1988).
- [77] David Garfinkle, Gary T. Horowitz, and Andrew Strominger, Charged black holes in string theory, *Phys. Rev. D* **43**, 3140 (1991); **45**, 3888(E) (1992).
- [78] Gary T. Horowitz and Andrew Strominger, Black strings and P-branes, *Nucl. Phys.* **B360**, 197 (1991).

- [79] Renata Kallosh and Tomas Ortin, Charge quantization of axion—dilaton black holes, *Phys. Rev. D* **48**, 742 (1993).
- [80] *Black Holes: The Membrane Paradigm*, edited by Kip S. Thorne, R. H. Price, and D. A. Macdonald (Yale University Press, New Haven, USA, 1986), ISBN 978-0-300-03770-8.
- [81] Dimitrios Psaltis, Delphine Perrodin, Keith R. Dienes, and Irina Mocioiu, Kerr black holes are not unique to general relativity, *Phys. Rev. Lett.* **100**, 091101 (2008).
- [82] Kenta Hioki and Umpei Miyamoto, Hidden symmetries, null geodesics, and photon capture in the Sen black hole, *Phys. Rev. D* **78**, 044007 (2008).
- [83] Parthapratim Pradhan, Thermodynamic products for Sen black hole, *Eur. Phys. J. C* **76**, 131 (2016).
- [84] Minyong Guo, Shupeng Song, and Haopeng Yan, Observational signature of a near-extremal Kerr-Sen black hole in the heterotic string theory, *Phys. Rev. D* **101**, 024055 (2020).
- [85] Rashmi Uniyal, Hemwati Nandan, and K. D. Purohit, Null geodesics and observables around the Kerr–Sen black hole, *Classical Quantum Gravity* **35**, 025003 (2018).
- [86] Galin N. Gyulchev and Stoytcho S. Yazadjiev, Kerr-Sen dilaton-axion black hole lensing in the strong deflection limit, *Phys. Rev. D* **75**, 023006 (2007).
- [87] Jincheng An, Jun Peng, Yan Liu, and Xing-Hui Feng, Kerr-Sen black hole as accelerator for spinning particles, *Phys. Rev. D* **97**, 024003 (2018).
- [88] Ziri Younsi, Alexander Zhidenko, Luciano Rezzolla, Roman Konoplya, and Yosuke Mizuno, New method for shadow calculations: Application to parametrized axisymmetric black holes, *Phys. Rev. D* **94**, 084025 (2016).
- [89] Yosuke Mizuno, Ziri Younsi, Christian M. Fromm, Oliver Porth, Mariafelicia De Laurentis, Hector Olivares, Heino Falcke, Michael Kramer, and Luciano Rezzolla, The current ability to test theories of gravity with black hole shadows, *Nat. Astron.* **2**, 585 (2018).
- [90] Sérgio Vinicius M. C. B. Xavier, Pedro V. P. Cunha, Luís C. B. Crispino, and Carlos A. R. Herdeiro, Shadows of charged rotating black holes: Kerr–Newman versus Kerr–Sen, *Int. J. Mod. Phys. D* **29**, 2041005 (2020).
- [91] Ashutosh Tripathi, Biao Zhou, Askar B. Abdikamalov, Dimitry Ayzenberg, and Cosimo Bambi, Constraints on Einstein–Maxwell dilaton-axion gravity from x-ray reflection spectroscopy, *J. Cosmol. Astropart. Phys.* **07** (2021) 002.
- [92] Soumya Jana and Sayan Kar, Shadows in dyonic Kerr-Sen black holes, *Phys. Rev. D* **108**, 044008 (2023).
- [93] Samuel E. Gralla, Daniel E. Holz, and Robert M. Wald, Black hole shadows, photon rings, and lensing rings, *Phys. Rev. D* **100**, 024018 (2019).
- [94] Marek Rogatko, Positivity of energy in Einstein–Maxwell axion dilaton gravity, *Classical Quantum Gravity* **19**, 5063 (2002).
- [95] Chandrima Ganguly and Soumitra SenGupta, Penrose process in a charged axion–dilaton coupled black hole, *Eur. Phys. J. C* **76**, 213 (2016).
- [96] A. Garcia, D. Galtsov, and O. Kechkin, Class of stationary axisymmetric solutions of the Einstein–Maxwell dilaton—axion field equations, *Phys. Rev. Lett.* **74**, 1276 (1995).
- [97] A. M. Ghezelbash and H. M. Siahhaan, Hidden and generalized conformal symmetry of Kerr-Sen spacetimes, *Classical Quantum Gravity* **30**, 135005 (2013).
- [98] Canisius Bernard, Stationary charged scalar clouds around black holes in string theory, *Phys. Rev. D* **94**, 085007 (2016).
- [99] S. Yazadjiev, Exact static solutions in four-dimensional Einstein–Maxwell dilaton gravity, *Int. J. Mod. Phys. D* **08**, 635 (1999).
- [100] J. M. Bardeen, Timelike and null geodesics in the Kerr metric, in *Proceedings, Ecole d'Eté de Physique Théorique: Les Astres Occlus: Les Houches, France, 1972* (1973), pp. 215–240.
- [101] Brandon Carter, Global structure of the Kerr family of gravitational fields, *Phys. Rev.* **174**, 1559 (1968).
- [102] A de Vries, The apparent shape of a rotating charged black hole, closed photon orbits and the bifurcation set  $A_4$ , *Classical Quantum Gravity* **17**, 123 (1999).
- [103] Naoki Tsukamoto, Zilong Li, and Cosimo Bambi, Constraining the spin and the deformation parameters from the black hole shadow, *J. Cosmol. Astropart. Phys.* **06** (2014) 043.
- [104] Leonardo Balart and Elias C. Vagenas, Regular black holes with a nonlinear electrodynamics source, *Phys. Rev. D* **90**, 124045 (2014).
- [105] Muhammed Amir and Sushant G. Ghosh, Shapes of rotating nonsingular black hole shadows, *Phys. Rev. D* **94**, 024054 (2016).
- [106] Naoki Tsukamoto, Black hole shadow in an asymptotically-flat, stationary, and axisymmetric spacetime: The Kerr–Newman and rotating regular black holes, *Phys. Rev. D* **97**, 064021 (2018).
- [107] Ramesh Narayan, Michael D. Johnson, and Charles F. Gammie, The shadow of a spherically accreting black hole, *Astrophys. J. Lett.* **885**, L33 (2019).
- [108] Andrew Chael, Michael D. Johnson, and Alexandru Lupsasca, Observing the inner shadow of a black hole: A direct view of the event horizon, *Astrophys. J.* **918**, 6 (2021).
- [109] Cosimo Bambi, Katherine Freese, Sunny Vagnozzi, and Luca Visinelli, Testing the rotational nature of the supermassive object M87\* from the circularity and size of its first image, *Phys. Rev. D* **100**, 044057 (2019).
- [110] Sarah Bird, William E. Harris, John P. Blakeslee, and Chris Flynn, The inner halo of M87: A first direct view of the red-giant population, *Astron. Astrophys.* **524**, A71 (2010).
- [111] John P. Blakeslee, Andres Jordan, Simona Mei, Patrick Cote, Laura Ferrarese, Leopoldo Infante, Eric W. Peng, John L. Tonry, and Michael J. West, The ACS Fornax cluster survey. V. Measurement and recalibration of surface brightness fluctuations and a precise value of the Fornax–Virgo relative distance, *Astrophys. J.* **694**, 556 (2009).
- [112] Michele Cantiello *et al.*, A precise distance to the host Galaxy of the binary neutron star merger GW170817 using surface brightness fluctuations, *Astrophys. J.* **854**, L31 (2018).

- [113] Fabrizio Tamburini, Bo Thidé, and Massimo Della Valle, Measurement of the spin of the M87 black hole from its observed twisted light, *Mon. Not. R. Astron. Soc.* **492**, L22 (2020).
- [114] Karl Gebhardt and Jens Thomas, The black hole mass, stellar M/L, and dark halo in M87, *Astrophys. J.* **700**, 1690 (2009).
- [115] Karl Gebhardt *et al.*, A relationship between nuclear black hole mass and Galaxy velocity dispersion, *Astrophys. J.* **539**, L13 (2000).
- [116] Jonelle L. Walsh, Aaron J. Barth, Luis C. Ho, and Marc Sarzi, The M87 black hole mass from gas-dynamical models of space telescope imaging spectrograph observations, *Astrophys. J.* **770**, 86 (2013).
- [117] Tuan Do *et al.*, Relativistic redshift of the star S0-2 orbiting the Galactic center supermassive black hole, *Science* **365**, 664 (2019).
- [118] R. Abuter *et al.*, Mass distribution in the Galactic center based on interferometric astrometry of multiple stellar orbits, *Astron. Astrophys.* **657**, L12 (2022).
- [119] R. Abuter *et al.*, Detection of the Schwarzschild precession in the orbit of the star S2 near the Galactic centre massive black hole, *Astron. Astrophys.* **636**, L5 (2020).
- [120] Roberto Abuter, A Amorim, M Bauböck, JP Berger, H Bonnet, W Brandner, Y Clénet, V Coudé Du Foresto, PT De Zeeuw, J Dexter *et al.*, A geometric distance measurement to the Galactic center black hole with 0.3% uncertainty, *Astron. Astrophys.* **625**, L10 (2019).
- [121] Kazunori Akiyama *et al.*, First M87 event horizon telescope results. VI. The shadow and mass of the central black hole, *Astrophys. J.* **875**, L6 (2019).
- [122] Indrani Banerjee, Bhaswati Mandal, and Soumitra SenGupta, Implications of Einstein–Maxwell dilaton–axion gravity from the black hole continuum spectrum, *Mon. Not. R. Astron. Soc.* **500**, 481 (2020).
- [123] Indrani Banerjee, Bhaswati Mandal, and Soumitra SenGupta, Signatures of Einstein–Maxwell dilaton–axion gravity from the observed jet power and the radiative efficiency, *Phys. Rev. D* **103**, 044046 (2021).